International Journal of Polymer Science

# Functional Polymer-Based Triggered Drug Delivery Systems

Lead Guest Editor: Can Yang Zhang
Guest Editors: Juan Li and Wenjing Lin

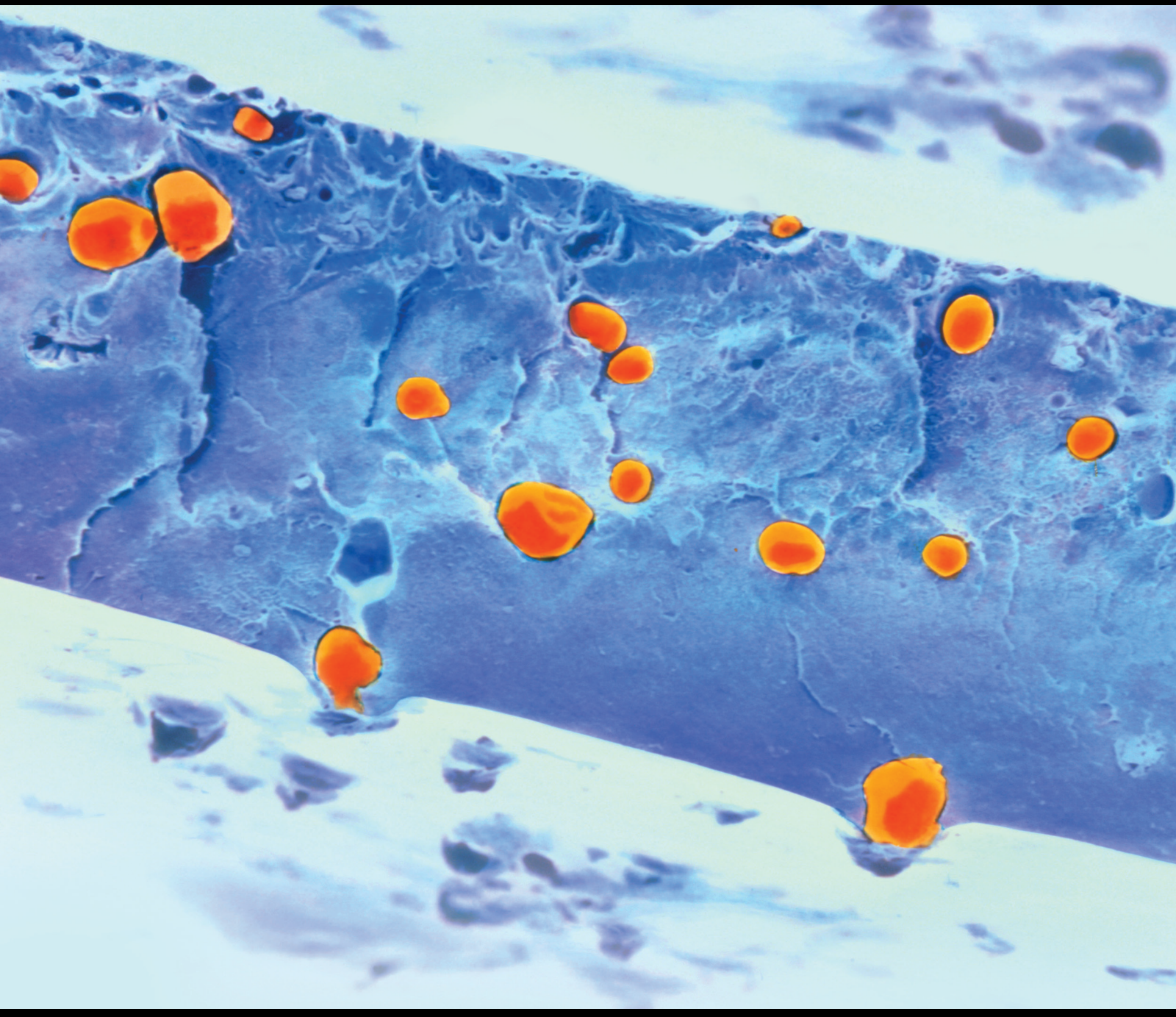

# Functional Polymer-Based Triggered Drug Delivery Systems

International Journal of Polymer Science

# Functional Polymer-Based Triggered Drug Delivery Systems

Lead Guest Editor: Can Yang Zhang
Guest Editors: Juan Li and Wenjing Lin

# Contents

**Multicomponent Nanocomposites for Complex Anticancer Therapy: Effect of Aggregation Processes on Their Efficacy**
Nataliya Kutsevol, Yuliia Kuziv, Tetiana Bezugla, Vasyl Chumachenko, and Vasyl Chekhun
Research Article (7 pages), Article ID 9627954, Volume 2020 (2020)

**Hydrogels Loaded with Methylene Blue: Sorption-Desorption and Antimicrobial Photoactivation Study**
O. Nadtoka, P. Virych, and N. Kutsevol
Research Article (6 pages), Article ID 9875290, Volume 2020 (2020)

**Isoflurane Regulates Proliferation, Apoptosis, and Inflammatory Response of Lipopolysaccharide-Induced Human Astrocyte through the miR-206/BDNF Axis**
Jianying Wang, Zhiyuan Liu, Xue Wang, and Yu Liu
Research Article (8 pages), Article ID 8109294, Volume 2020 (2020)

***Cyclocarya paliurus* Polysaccharide Inhibits Glioma Cell U251 Proliferation, Migration, and Invasion and Promotes Apoptosis via the GSK3$\beta$/$\beta$-Catenin Signaling Pathway**
Xiaolong Du, Kai Guo, Yongqian Ma, and Jianyong Chang
Research Article (9 pages), Article ID 2391439, Volume 2020 (2020)

**Effect of $Mn_3O_4$ Nanoparticles on Lipopolysaccharide-Induced Inflammatory Factors in the Human Tendon Cells and Its Mechanism**
Shangjun Fu, Zongyun He, Yongfeng Tang, and Bo Lan
Research Article (8 pages), Article ID 1934732, Volume 2020 (2020)

Hindawi
International Journal of Polymer Science
Volume 2020, Article ID 9627954, 7 pages
https://doi.org/10.1155/2020/9627954

*Research Article*

# Multicomponent Nanocomposites for Complex Anticancer Therapy: Effect of Aggregation Processes on Their Efficacy

**Nataliya Kutsevol**,[1] **Yuliia Kuziv**,[1] **Tetiana Bezugla**,[1] **Vasyl Chumachenko**,[1] **and Vasyl Chekhun**[2]

[1]*Taras Shevchenko National University of Kyiv, 60 Volodymyrska Str., 01602 Kyiv, Ukraine*
[2]*R.E. Kavetsky Institute of Experimental Pathology, Oncology and Radiobiology, 45 Vasylkivska Str., 03022 Kyiv, Ukraine*

Correspondence should be addressed to Yuliia Kuziv; garaguts.yulia.fox@gmail.com

Received 7 February 2020; Revised 14 April 2020; Accepted 20 April 2020; Published 5 May 2020

Guest Editor: Can Yang Zhang



Multicomponent nanocomposites for anticancer therapy were prepared, characterized, and tested for their antitumor efficacy. The water-soluble star-like dextran-graft-polyacrylamide copolymer was used as a nanoplatform for the creation of polymer-based multicomponent drug delivery systems for photodynamic and combined (photodynamic+chemotherapy) antitumor therapy. The three-component nanocomposites with incorporated gold nanoparticles and photosensitizer and the four-component ones additionally loaded by Doxorubicin into polymer nanoplatform were studied at 25 and 37°C by transmission electron microscopy and dynamic light scattering. Nanocomposites were tested for their photodynamic cytotoxicity for the cell line of breast cancer MCF-7/S. Three-component nanocomposites demonstrated higher efficacy than the four-component ones. The decrease in the activity of the four-component systems is explained by the aggregation process caused by the introduction of an additional component, which leads to a decrease in the hydrophilic-hydrophobic balance of the polymer macromolecule.

## 1. Introduction

Actual cancer statistics indicate the need for innovative approaches, including nanotechnology, for efficient cancer diagnosis and therapy. Currently, the malignant tumor treatments use radiation, overheating (hyperthermia), excess oxygen (hyperoxygenation), and some harmful chemical substances or mutagens [1]. To improve treatment methods, researchers combine various inhibitory effects on cancer cells. Sometimes, anticancer drugs use several ways to destroy tumors [2].

In photothermal therapy (PTT) and photodynamic therapy (PDT), the desired effects of heat generation by metal nanoparticles and activation of photosensitizers (PS) occur in response to applied irradiation with specific light wavelengths. Recent studies have shown a synergistic effect obtained by the simultaneous use of PTT and PDT [3, 4]. Cytotoxic photothermal heating together with reactive singlet oxygen can trigger apoptotic and necrotic cancer cell death [2, 5]. The combination of multifunctional plasmonic nanoparticles and fluorescent photodynamic agents activated by near-infrared lasers has been the subject of research with encouraging results [3–6].

Gold nanoparticles (AuNPs) are known to be a photothermal agent with good biocompatibility and chemical inactivity. Their surface plasmon resonance (SPR) effect is highly efficient in converting light to heat, which leads to hyperthermia [7]. The SPR peak of AuNPs can be adjusted to the near-infrared region by controlling the geometrical parameters of the particles, such as size and shape [8]. Hyperthermia-induced cytotoxicity occurs within 1 h at 42°C, which can be shortened using higher temperatures [9]. Also, AuNPs can be easily accumulated in the tumor tissue due to the increased permeability and retention effect of the tumor [10].

Being incorporated into the cancer cells, AuNPs increase the reactive oxygen species generated by the cells, thereby affecting cell function [11]. However, AuNPs are more commonly used as carriers of photosensitizers. The molecules of

most photosensitizers are hydrophobic, and they require delivery systems to accomplish their cancer therapeutic effects [12, 13]. To increase the accumulation of PS in the tumor, it is advisable to combine it with gold nanoparticles, which are tropical to the tumor tissue and can serve as carriers of PS molecules [10]. Some of the scientific groups have reported that gold nanoparticles enhance not only the accumulation of PS but also the development of reactive oxygen species [14]. They demonstrated that complex compound AuNPs/photosensitizer/phase transfer reagents achieved higher singlet oxygen species generation compared to free photosensitizers [15].

Modern advances in drug delivery are now predicated upon water-soluble polymers with special characteristics in a soluble state [7, 10]. These polymers can be promising carriers not only for cytotoxic molecules but also for different nanosized objects. There is evidence of using polymer carriers for metal nanoparticles and hydrophobic organic substances simultaneously [16]. Polymer nanosystems are generated to achieve controlled drug release and target the delivery of hydrophobic drugs [17, 18]. In some cases, the conjecturable harmful effects on cancer cells can be enhanced by using polymer-drug conjugates with mutually reinforcing components. As it was shown in *in vitro* experiments on malignant cell line MT-4, a nanocomposite consisting of AuNPs and photosensitizer Chlorin e6 in a dextran-graft-polyacrylamide matrix demonstrated a twofold increase of photodynamic efficiency compared to a free photosensitizer [19].

Nanotechnology allows creating novel multicomponent drug delivery systems consisting of several components, for example, metal nanoparticles, photosensitizer, and anticancer chemical agent incorporated into the polymer matrix. Here, we focused on the synthesis and study of nanocomposites containing AuNPs for PTT, Chlorin e6 for PDT, and Doxorubicin for chemotherapy loaded into a water-soluble polyacrylamide-based polymer. The main purpose of the study was to understand the process occurring during the formation of multicomponent nanosystems at physiological temperatures (25 and 37°C).

## 2. Materials and Methods

### 2.1. Polymer Nanocarrier and Nanosystem Syntheses

*2.1.1. Reagents.* Tetrachloroauric acid, sodium borohydride, and Hank's balanced salt solution were purchased from Sigma-Aldrich (USA). Dimethyl sulfoxide (DMSO) was obtained from Serva (Germany). All reagents were of analytical purity and were used without further purification.

Chlorin e6 (Ce6) (Santa Cruz Biotechnology, USA) and Doxorubicin hydrochloride (Dox) (Sigma-Aldrich, USA) were used without further purification.

Double distilled water was used when needed.

*2.1.2. Polymer Nanocarrier.* Copolymer dextran-graft-polyacrylamide (D-g-PAA) in anionic form was used as a polymer matrix for gold nanoparticle synthesis as well as for the fabrication of nanosystems loaded with AuNPs, photosensitizer Ce6, and Dox. Synthesis and peculiarities of the macromolecular structure of star-like copolymer D-g-PAA were discussed in detail in [20]. D-g-PAA has dextran core (Mw = 70 · 105 g/mol) and five grafted PAA chains. The average molecular weight of D-g-PAA (Mw) is equal to $2.15 \cdot 10^6$ g/mol, a radius of gyration (Rg) 85 nm, and polydispersity (Mw/Mn) 1.75. The anionic form of this copolymer was obtained via alkaline hydrolysis: 2 g of D-g-PAA was dissolved in 200 ml of distilled water, and then, the required amount of NaOH solution was added to it. The mixture was kept in a water bath at 50°C. The probes were taken in 30 min and precipitated by acetone. All samples were freeze-dried.

Size-exclusion chromatography coupled with light scattering was used for polymer sample characterization. SEC analysis was carried out by using a multidetection device consisting of an LC-10AD Shimadzu pump (throughput $0.5\ \mathrm{ml \cdot mn^{-1}}$), an automatic injector WISP 717+ from Waters, 3 coupled 30 cm-Shodex OH-pak columns (803HQ, 804HQ, and 806HQ), a multiangle light scattering detector DAWN F from Wyatt Technology, and a differential refractometer R410 from Waters. Distilled water containing 0.1 M $NaNO_3$ was used as eluent. The degree of conversion of nonionic samples to ionic form was analyzed using a potentiometric titration of hydrolyzed samples. The content of carboxylate groups for hydrolyzed copolymer was approximately 37% [20]. Hereinafter, the copolymer D-g-PAA in the anionic form will be designated as Polymer.

*2.1.3. Synthesis of Nanosystem Polymer/AuNPs.* AuNPs were synthesized by the chemical reduction of Au precursor (tetrachloroauric acid) in aqueous Polymer solution at 25°C. Firstly, 0.05 ml of tetrachloroauric acid solution (0.1 M) was added to 1 ml of Polymer solution (1 mg/ml) and stirred for 20 min. Then, 0.1 ml of aqueous $NaBH_4$ solution (0.1 M) was injected. The final solution turned ruby red thus indicating the formation of AuNPs. The Au sol is designated as Polymer/AuNPs throughout.

*2.1.4. Synthesis of Nanosystem Polymer/AuNPs/Ce6.* A photosensitizer Ce6 is a poor water-soluble substance [21], so a stock solution of Ce6 (0.182 mg/ml) was prepared in DMSO. Then, 0.55 ml of this solution was mixed with 0.27 ml of distilled water. Finally, this mixture was added to 1.15 ml of Polymer/AuNP nanosystem under constant stirring. Thus, a three-component nanosystem was obtained, and it is designated as Polymer/AuNPs/Ce6.

*2.1.5. Synthesis of Nanosystem Polymer/AuNPs/Dox.* To prepare a three-component nanosystem containing a chemotherapeutic drug, 0.27 ml of the Dox solution (0.147 mg/ml) was mixed with 0.55 ml of distilled water; then, this mixture was added to 1.15 ml of Au sol (Polymer/AuNPs) under constant stirring. This system is designated as Polymer/AuNPs/Dox.

*2.1.6. Synthesis of Nanosystem Polymer/AuNPs/Ce6/Dox.* Four-component nanosystem was prepared using the Au sol synthesized in the Polymer solution. 0.27 ml of Dox (0.147 mg/ml) and 0.55 ml of Ce6 (0.182 mg/ml) solutions

were added to 1.15 ml of Polymer/AuNP solution under constant stirring. This system is designated as Polymer/AuNPs/Ce6/Dox.

*2.2. Methods*

*2.2.1. Transmission Electron Microscopy (TEM).* The observations of the AuNPs were carried out employing two TEMs, Tecnai G2 (ssCCD Eagle Camera) and CM12 (FEI, Eindhoven Netherlands) (Megaview SIS Camera). Copper grids with a plain carbon film were used for sample preparation (Elmo, Cordouan Technologies, Bordeaux, France). A 5 $\mu$l drop was deposited and let adsorbed for 1 min, and then, the excess of the solution was removed with a piece of filter paper.

*2.2.2. Dynamic Light Scattering (DLS).* DLS measurements were carried out using Zetasizer Nano ZS90 (Malvern Instruments Ltd., UK). The apparatus contains a 4 mW He-Ne laser with a wavelength of 632.8 nm. The scattered light is detected at an angle of 173° (backscattering).

Three-component nanosystems Polymer/AuNPs/Ce6 and Polymer/AuNPs/Dox and four-component nanosystem Polymer/AuNPs/Ce6/Dox were studied by DLS at 25 and 37°C. At the indicated temperature, the samples are kept for 5 minutes to achieve equilibrium. At least 10 correlation curves for each temperature point were processed by the CONTIN algorithm [22]. This is known to be reliable for complex systems to obtain hydrodynamic diameter (HD) distributions [23].

For correct analysis of processes occurring in multicomponent nanosystems, the authors' program or data treatment was used [24].

*2.2.3. Evaluation of Dark Cytotoxicity and Photocytotoxic Activity of Nanocomposites.* The cell line of breast cancer MCF-7/S was used for the experiments. The samples were obtained from a cell bank of human and animal tissue lines of the R.E. Kavetsky Institute of Experimental Pathology, Oncology and Radiobiology of National Academy of Sciences of Ukraine. Suspension cultures were grown in vitro in a complete nutrient medium of RPMI 1640 (Sigma-Aldrich, USA) with 2% L-glutamine, 10% embryonic serum calf (ETC; Biowest, France), and 40 $\mu$g/ml gentamicin at 37°C and in a humid atmosphere with the content of 5% $CO_2$. For the evaluation of dark cytotoxicity of nanoparticles and nanocomposites, the calculation of live/dead cells was determined in the MTT test after their staining with trypan blue [25].

For the *in vitro* study of the photodynamic effect of nanocomposites, the cells were incubated with nanosystems of different compositions for 1.5 h at 37°C. The samples were washed three times from unbound PS and irradiated in a Hanks solution with laser light. After that, the cells were transferred to the culture medium and incubated for 18-20 h at 37°C for the development and completion of apoptosis or necrosis in them. Then, the cell viability was determined in the MTT test. Each experiment was repeated at least 5 times.

A semiconductor laser (PMNP Photonikik Plus, Cherkasy) with a wavelength of 660 nm, which coincides with one of the Ce6 absorption maxima, was used as a light source for photodynamic damage to cells.

## 3. Results and Discussion

It was reported [26, 27] that D-g-PAA copolymers in both nonionic and anionic forms are not cytotoxic, and they can be absorbed by murine macrophages. These polymers were used as a base for the creation of the hybrid composites containing gold nanoparticles. The systems obtained were examined against breast cancer MCF-7 cell line and MT-4 (human T-cell leukemia) cell line [28]. The results proved low *in vitro* toxicity of examined composite like Polymer/AuNP sample even in high doses.

Our recent studies have shown higher photodynamic *in vivo* and *in vitro* efficiency against MT-4 cells (human T-cell leukemia) of a nanocomposite containing AuNPs and photosensitizer Ce6 incorporated into the star-like copolymer D-g-PAA in the anionic form in comparison with the same nanocomposite based on the nonionic polymer counterpart [26]. Also, the D-g-PAA copolymer in anionic form has demonstrated high efficiency as a nanocarrier for anticancer drugs Cisplatin and Doxorubicin when tested against K-562 (human chronic myelogenous leukemia cell line), U-937 (human histiocytic lymphoma cell line), and HeLa cells (cervical cancer) [27, 29]. Thus, the idea was to create nanocomposite for complex photothermal, photodynamic, and chemotherapy, namely, to synthesize Polymer-based nanocomposite loaded with AuNPs, photosensitizer Chlorin e6, and anticancer drug Doxorubicin hydrochloride simultaneously.

For the synthesis of the D-g-PAA copolymers, the cerium-ion-induced redox initiation method was used [20]. The average number of grafts per dextran molecule ($n$) is dependent on the ratio of Ce(IV) ions to dextran molecules [20]; this value was equal to 5. The mechanism of Ce(IV) initiation is based on the formation of the chelate complex, which while decomposing generates free radical sites on the polysaccharide backbone. These active free radicals trigger PAA chain growth in the presence of an acrylic monomer. The reaction path is shown below:

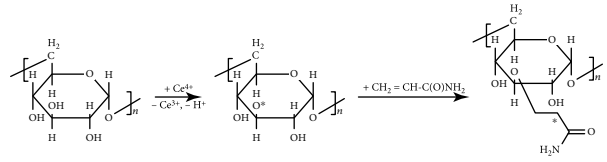


The peculiarities of the molecular structure of branched copolymers dextran-graft-polyacrylamide in nonionic and ionic forms were discussed in [20]. These copolymers are star-like, consisting of the dextran core and long polyacrylamide grafts. The average conformation of grafted PAA chains depends on the grafting ratio. For the D-g-PAA copolymer used in the present work, the PAA grafts have worm-like conformation. The ionic form of this copolymer was obtained after saponification. The branched polyelectrolyte has an extremely expanded conformation of the grafted chains in solution [20]. Alkaline hydrolysis of D-g-PAA

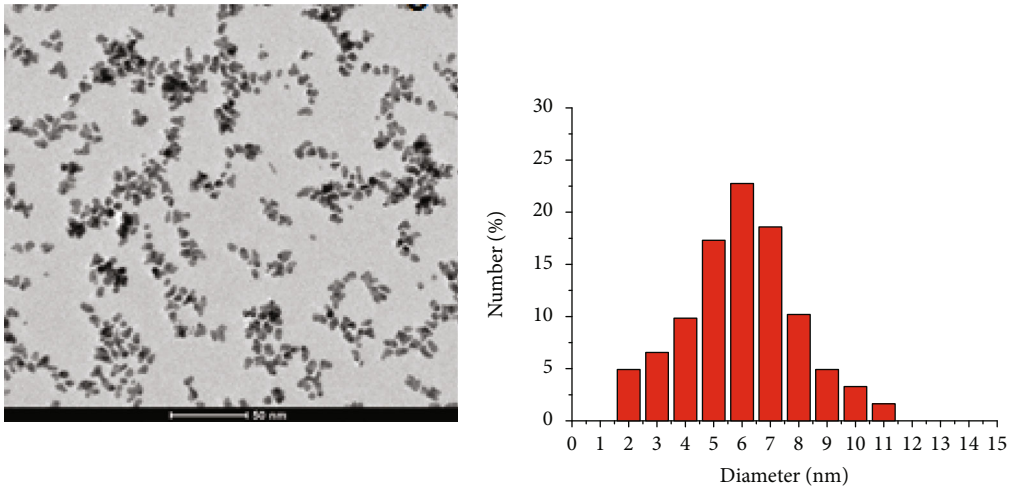


(a) (b)

Figure 1: TEM image of AuNPs in Polymer/AuNP nanosystem (a) and size distribution histogram of AuNPs in this sample (b).

copolymers was not accompanied by irrelevant processes (the breaking or cross-linking of macromolecules) as was confirmed by SEC analysis of source and saponified samples. The branched polymers have a higher local concentration of functional groups in comparison with their linear analogs. These structural peculiarities are advantageous for biomedical applications [20].

AuNPs were synthesized *in situ* in a water solution of D-g-PAA in the anionic form. According to the TEM data, the Polymer/AuNP system contains gold particles of 2-11 nm in size with not completely spherical shape (Figure 1(a)). The size distribution of AuNPs is shown in Figure 1(b).

DLS analysis of heterogeneous Polymer/AuNP solution revealed several scattering objects that can be divided into two groups with well-defined maxima. According to the molecular parameter of the polymer matrix represented above, the peak with a maximum at 70 nm (Figure 2) corresponds to the macromolecules of D-g-PAA in anionic form loaded with AuNPs. The weakly pronounced peaks in the region of 2-11 nm on the weighted intensity distribution can be attributed to AuNPs. The scattering intensity of small metal nanoparticles about 10 nm in size is drastically lower in comparison with large polymer coils [30]. That is why the intensity distribution for small nanoparticles does not allow evaluating the average size and polydispersity of AuNPs in nanosystems by using DLS.

Three-component Polymer/AuNPs/Ce6 and Polymer/-AuNPs/Dox and four-component Polymer/AuNPs/Ce6/Dox nanosystems were prepared by the method described above, then were centrifuged. The absorption spectra of the supernatant showed the absence of Ce6 and Dox in solution, thus indicating its total incorporation into polymer nanocarrier. These nanocomposites were used for DLS and *in vitro* anticancer examination.

The size distributions of scattering nanoobjects in the three-component Polymer/AuNPs/Ce6 nanosystem at different temperatures are shown in Figures 3(a) and 3(b). DLS data demonstrate several types of scattering nanoobjects

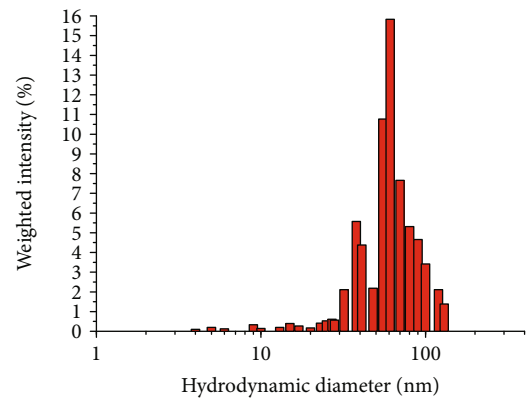


Figure 2: Hydrodynamic diameter distributions of scattering objects in Polymer/AuNP nanosystem.

in this system at 25°C (Figure 3(a), black curve). The first maximum corresponds to AuNPs of about 10 nm in size. The second maximum can be attributed to the individual AuNP-loaded macromolecules with coil diameter near 70-80 nm. The third maximum deals with the presence of aggregates of macromolecules with AuNPs inside. The size of these nanoobjects is equal to 200-500 nm. Changes in dimensional characteristics of this nanosystem occur at 37°C. Two distinct peaks are registered in the size range above 100 nm thus indicating the reorganization of aggregates (Figure 3(b), black curve). In contrast to other nanosystems, the fraction of aggregates with the less sizes (100-200 nm) in Polymer/-AuNPs/Ce6 system is significant. That may be caused by the partial destruction of hydrogen bonds between grafts of polymer nanocarrier at 37°C. However, the size of the gold nanoparticles and the size of nanoobjects corresponding to individual macromolecules with incorporated AuNPs do not change.

According to DLS data obtained from an experiment with Polymer/AuNPs/Dox nanosystem at 25°C, this sample contains AuNPs of 10 nm in size, individual Polymer

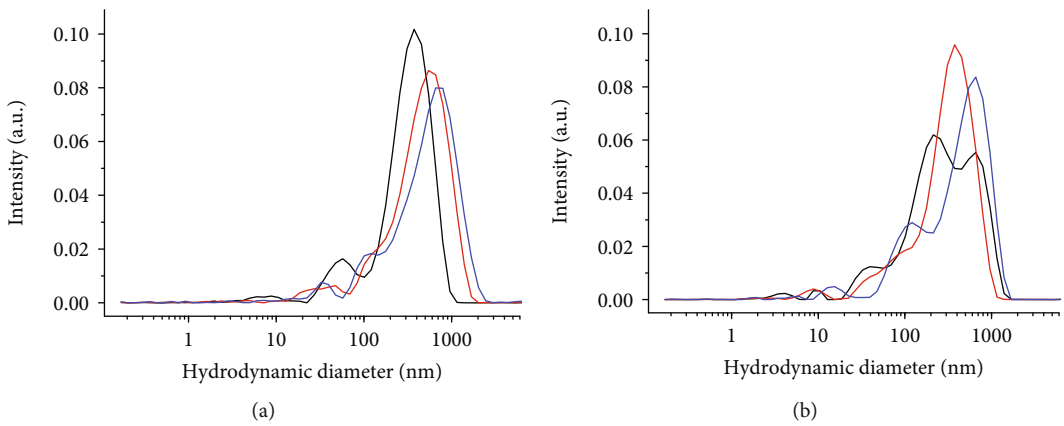


Figure 3: The dependence of the normalized scattering intensity on the hydrodynamic diameter of the scattering objects for the Polymer/AuNPs/Ce6 (black), Polymer/AuNPs/Dox (red), and Polymer/AuNPs/Ce6/Dox (blue) nanosystems at 25°C (a) and 37°C (b).

Table 1: Composition of nanocomposites used for in vitro tests on MCF-7/S breast cancer cells.

| Sample | $C_{Polymer}$ (mkg/ml) | $C_{AuNPs}$ (mkg/ml) | $C_{Ce6}$ (mkg/ml) | $C_{Dox}$ (mkg/ml) |
|---|---|---|---|---|
| Nanocomposite 1 | 508 | 500 | 50 | — |
| Nanocomposite 2 | 508 | 500 | 50 | 20 |
| Nanocomposite 3 | 508 | 500 | 50 | 20 (extempore) |

macrocoils with incorporated AuNPs (60-70 nm), and its macromolecular aggregates (approximately 100-110 nm and 500 nm) (Figure 3(a), red curve). Compared to Polymer/-AuNPs/Ce6 nanosystem, the aggregation process in Polymer/AuNPs/Dox nanosystem is more significant. With an increase in temperature to 37°C, changes in the dimensional characteristics of nanosystems are registered, namely, the reduction in the size of the greatest aggregates occurs (Figure 3(b), red curve). These changes could be caused by two processes—the destruction of some aggregates or the compression of macromolecular coils. However, the latter process seems unlikely because no additional component that could bind to the functional groups of the polymer was added. The size of the AuNPs and the size of the nanoobjects, which consist of individual macromolecules with incorporated AuNPs, do not change.

For Polymer/AuNPs/Ce6/Dox nanosystem, there are several scattering objects on the DLS curve at 25°C (Figure 3(a), blue curve). AuNPs of 10 nm in size, individual macromolecules with incorporated AuNPs (about 60-70 nm), and its aggregates (100-200 nm and about 800 nm) can be observed. The increased ability to aggregate in this nanosystem compared to those described above seems to be the result of an increase in the number of components included in the Polymer macrocoils. That leads to a change in the hydrophobic-hydrophilic balance of the Polymer molecules. Polymer loaded with considered components become more hydrophobic since hydrophilic acrylamide and carboxylate groups are blocked both by Ce6 and Dox molecules.

There are no significant changes in sizes of scattering objects for Polymer/AuNPs/Ce6/Dox nanosystem at 37°C. Only some decreases of the hydrodynamic radius of the greatest aggregates are observed (Figure 3(b), blue curve). It can be caused by reorganization in the nanosystems due to the partial destruction of internal and external hydrogen bonds between grafts of polymer nanocarrier. The size of AuNPs and the size of the nanoobjects consisting of individual macromolecules with AuNPs do not change. However, an increase in aggregation ability in a four-component nanosystem in comparison with three-component ones at studied temperatures is evident. As a whole, four-component nanosystem Polymer/AuNPs/Ce6/-Dox contains macromolecular aggregates that are greater in size compared to those in both Polymer/AuNPs/Ce6 and Polymer/AuNPs/Dox nanosystems.

Polymer/AuNP/Ce6 and Polymer/AuNPs/Ce6/Dox nanosystems were tested for its PDT and dark cytotoxicity on MCF-7/S breast cancer cells. The compositions of tested nanosystems are shown in Table 1. Nanocomposite 1 and Nanocomposite 2 were presynthesized and kept in the refrigerator. Nanocomposite 3 was prepared by "extempore" way through the addition of Dox to the Polymer/AuNPs/Ce6 composition in 10 minutes before its mixing with the culture cells. As was shown, the individual Polymer and Polymer loaded with AuNPs have no significant cytotoxic effects on the cancer cells at the studied concentrations.

In the "control" experiment, the cancer cells were subjected to the same manipulations but without the addition of nanocomposites. It was shown that MCF-7/S cells were not sensitive to Nanocomposites 1 and 2 without external irradiation (Figure 4, blue bars). The "dark" measures demonstrated the same results on the survival of cells being incubated with the addition of the studied nanocomposites and in the "control" experiment.

However, a significant increase in the toxic properties of Nanocomposite 1 was registered after PDT (Figure 4, red

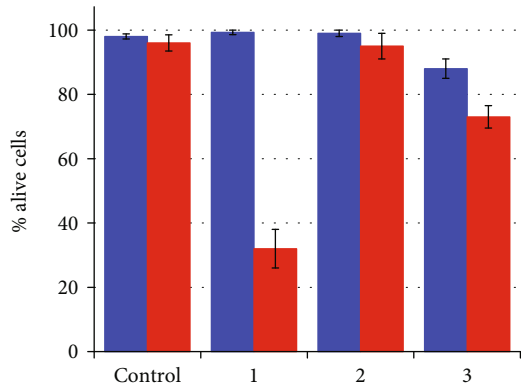


Figure 4: The survival of MCF-7/S cells after treatment with Nanocomposite 1 (1); Nanocomposite 2 (2); and Nanocomposite 3 (3) and in control experiment (control). Blue: "dark" measures; red: after PDT.

bars). Nanocomposite 2 contains the same amount of Ce6 as Nanocomposite 1, but the survival of cells after external irradiation is much higher for Nanocomposite 2 compared to Nanocomposite 1. The significant decrease in the efficiency of the four-component Nanocomposite 2 compared to the three-component Nanocomposite 1 may be a result of an increased aggregation of macromolecular coils containing the active ingredients of the system. Nanocomposite 3, prepared "ex tempore," demonstrated higher efficacy in comparison with Nanocomposite 2, despite the same content of ingredients. It may be due to the fact that the molecules of Dox-added extempore are not completely incorporated into polymer in 10 min. The system does not achieve equilibrium. Therefore, free Dox can be present in Nanosystem 3 that explains some "dark" toxicity effect for tumor cells as well as higher results on the cell death in the PDT experiment (Figure 4, blue bars).

Similar effects of decreasing efficiency of polymer nanosystems loaded with active components towards damage of cancer cells were revealed when the number of these components increased [31]. As it was reported in [27], the water-soluble polymer nanocarriers such as dextran-graft-(polyacrylamide-co-polyacrylic acid) loaded with chemotherapeutic substance Cisplatin demonstrated high toxicity to cancer cells. However, when the copolymers were conjugated with both AgNPs and Cisplatin, the three-component nanosystem showed a lower cytotoxic effect [27], which was caused by the aggregation process in multicomponent systems.

## 4. Conclusion

It is shown in the current work that the polymer-based multicomponent nanosystem Polymer/AuNPs/Ce6 demonstrated high efficacy in PDT, but the addition of the fourth component Dox to this composite resulted in a decrease of antitumor efficacy. The aggregation processes and formation of great aggregates in the four-component system Polymer/-AuNPs/Ce6/Dox seem to cause a decrease in the therapeutic effect in PDT.

The development of nanosystems for photodynamic therapy is in the focus of current biomedical research. It is possible to improve the effectiveness of cancer treatment due to the achievements of nanotechnology that provide an opportunity to develop complex therapeutic composites, but the use of multicomponent nanosystems needs a deep understanding of the processes occurring at its preparation to avoid some aggregation.

## Data Availability

The data used to support the findings of this study are included within the article.

## Conflicts of Interest

The authors declare that there is no conflict of interest regarding the publication of this paper.

## References

[1] D. Feldman, "Polymers and polymer nanocomposites for cancer therapy," *Applied Science*, vol. 9, no. 18, p. 3899, 2019.

[2] R. Mendes, P. Pedrosa, J. C. Lima, A. R. Fernandes, and P. V. Baptista, "Photothermal enhancement of chemotherapy in breast cancer by visible irradiation of gold nanoparticles," *Scientific Reports*, vol. 7, no. 1, p. 10872, 2017.

[3] F. Ghorbani, N. Attaran-Kakhki, and A. Sazgarnia, "The synergistic effect of photodynamic therapy and photothermal therapy in the presence of gold-gold sulfide nanoshells conjugated indocyanine green on HeLa cells," *Photodiagnosis and Photodynamic Therapy*, vol. 17, pp. 48–55, 2017.

[4] B. Jang, J.-Y. Park, C.-H. Tung, I.-H. Kim, and Y. Choi, "Gold nanorod-photosensitizer complex for near-infrared fluorescence imaging and photodynamic/photothermal therapy *in vivo*," *ACS Nano*, vol. 5, no. 2, pp. 1086–1094, 2011.

[5] H. Kim and D. Lee, "Near-infrared-responsive cancer photothermal and photodynamic therapy using gold nanoparticles," *Polymers*, vol. 10, no. 9, p. 961, 2018.

[6] S. Veeranarayanan, M. S. Mohamed, A. C. Poulose et al., "Photodynamic therapy at ultra-low NIR laser power and X-ray imaging using $Cu_3BiS_3$ nanocrystals," *Theranostics*, vol. 8, no. 19, pp. 5231–5245, 2018.

[7] P. Kaur, M. L. Aliru, A. S. Chadha, A. Asea, and S. Krishnan, "Hyperthermia using nanoparticles–promises and pitfalls," *International Journal of Hyperthermia*, vol. 32, no. 1, pp. 76–88, 2016.

[8] C. L. Nehl and J. H. Hafner, "Shape-dependent plasmon resonances of gold nanoparticles," *Journal of Materials Chemistry*, vol. 18, no. 21, pp. 2415–2419, 2008.

[9] S. H. Beachy and E. A. Repasky, "Toward establishment of temperature thresholds for immunological impact of heat exposure in humans," *International Journal of Hyperthermia*, vol. 27, no. 4, pp. 344–352, 2011.

[10] L. A. Bennie, H. O. McCarthy, and J. A. Coulter, "Enhanced nanoparticle delivery exploiting tumour-responsive formulations," *Cancer Nano*, vol. 9, no. 1, p. 10, 2018.

[11] J. Peng and X. Liang, "Progress in research on gold nanoparticles in cancer management," *Medicine*, vol. 98, no. 18, p. e15311, 2019.

[12] Y. N. Konan, R. Gurny, and E. Allémann, "State of the art in the delivery of photosensitizers for photodynamic therapy,"

*Journal of Photochemistry and Photobiology B: Biology*, vol. 66, no. 2, pp. 89–106, 2002.

[13] C. Yao, L. Zhang, J. Wang et al., "Gold nanoparticle mediated phototherapy for cancer," *Journal of Nanomaterials*, vol. 2016, Article ID 5497136, 29 pages, 2016.

[14] E. Paszko, C. Ehrhardt, M. O. Senge, D. P. Kelleher, and J. V. Reynolds, "Nanodrug applications in photodynamic therapy," *Photodiagnosis and Photodynamic Therapy*, vol. 8, no. 1, pp. 14–29, 2011.

[15] S. J. Chadwick, D. Salah, P. M. Livesey, M. Brust, and M. Volk, "Singlet oxygen generation by laser irradiation of gold nanoparticles," *The Journal of Physical Chemistry C*, vol. 120, no. 19, pp. 10647–10657, 2016.

[16] W. B. Liechty, D. R. Kryscio, B. V. Slaughter, and N. A. Peppas, "Polymers for drug delivery systems," *Annual Review of Chemical and Biomolecular Engineering*, vol. 1, no. 1, pp. 149–173, 2010.

[17] N. Jawahar and S. N. Meyyanathan, "Polymeric nanoparticles for drug delivery and targeting: a comprehensive review," *International Journal of Health & Allied Sciences*, vol. 1, no. 4, pp. 217–230, 2012.

[18] N. R. Jabir, S. Tabrez, G. M. Ashraf, S. Shakil, G. A. Damanhouri, and M. A. Kamal, "Nanotechnology-based approaches in anticancer research," *International Journal of Nanomedicine*, vol. 7, pp. 4391–4408, 2012.

[19] V. A. Chumachenko, I. O. Shton, E. D. Shishko, N. V. Kutsevol, A. I. Marinin, and N. F. Gamaleia, "Branched copolymers dextran-graft-polyacrylamide as nanocarriers for delivery of gold nanoparticles and photosensitizers to tumor cells," in *Nanophysics, Nanophotonics, Surface Studies, and Applications*, O. Fesenko and L. Yatsenko, Eds., vol. 183, pp. 379–390, Springer Proceedings in Physics, 2016.

[20] M. Bezugly, N. Kutsevol, M. Rawiso, and T. Bezugla, "Water-soluble branched copolymers dextran-polyacrylamide and their anionic derivates as matrices for metal nanoparticles in situ synthesis," *Chemik*, vol. 66, no. 8, pp. 865–867, 2012.

[21] V. P. Savitskiy, V. P. Zorin, and M. P. Potapnev, "Accumulation of chlorine e6 derivatives in cells with different level of expression and function activity of multidrug resistance protein P-gp 170," *Experimental oncology*, vol. 27, no. 1, pp. 47–51, 2005.

[22] S. Provencher, "CONTIN: a general purpose constrained regularization program for inverting noisy linear algebraic and integral equations," *Computer Physics Communications*, vol. 27, pp. 229–242, 1992.

[23] A. Scotti, W. Liu, J. S. Hyatt et al., "The CONTIN algorithm and its application to determine the size distribution of microgel suspensions," *The Journal of Chemical Physics*, vol. 142, no. 23, p. 234905, 2015.

[24] V. Chumachenko, N. Kutsevol, Y. Harahuts, M. Rawiso, A. Marinin, and L. Bulavin, "Star-like dextran-graft-PNiPAM copolymers. Effect of internal molecular structure on the phase transition," *Journal of Molecular Liquids*, vol. 235, pp. 77–82, 2017.

[25] A. K. Kwok, C. K. Yeung, T. Y. Lai, K. P. Chan, and C. P. Pang, "Effects of trypan blue on cell viability and gene expression in human retinal pigment epithelial cells," *The British Journal of Ophthalmology*, vol. 88, no. 12, pp. 1590–1594, 2004.

[26] N. Kutsevol, A. Naumenko, Y. Harahuts et al., "New hybrid composites for photodynamic therapy: synthesis, characterization and biological study," *Applied Nanoscience*, vol. 9, no. 5, pp. 881–888, 2019.

[27] G. Telegeev, N. Kutsevol, V. Chumachenko et al., "Dextran-polyacrylamide as matrices for creation of anticancer nanocomposite," *International Journal of Polymer Science*, vol. 2017, Article ID 4929857, 9 pages, 2017.

[28] N. Kutsevol, Y. Harahuts, I. Shton et al., "In vitro study of toxicity of hybrid gold-polymer composites," *Molecular Crystals and Liquid Crystals*, vol. 671, no. 1, pp. 1–8, 2018.

[29] A. Yurchenko, N. Nikitina, V. Sokolova et al., "A novel branched copolymer-containing anticancer drug for targeted therapy:*in vitro* research," *Bionanoscience*, vol. 10, pp. 249–259, 2019.

[30] J. Stetefeld, S. A. McKenna, and T. R. Patel, "Dynamic light scattering: a practical guide and applications in biomedical sciences," *Biophysical Reviews*, vol. 8, no. 4, pp. 409–427, 2016.

[31] N. Kutsevol, A. Naumenko, V. Chumachenko, O. Yeshchenko, Y. Harahuts, and V. Pavlenko, "Aggregation processes in hybrid nanosystem polymer/nanosilver/cisplatin," *Ukrainian Journal of Physics*, vol. 63, no. 6, pp. 513–520, 2018.

Hindawi
International Journal of Polymer Science
Volume 2020, Article ID 9875290, 6 pages
https://doi.org/10.1155/2020/9875290

*Research Article*

# Hydrogels Loaded with Methylene Blue: Sorption-Desorption and Antimicrobial Photoactivation Study

**O. Nadtoka, P. Virych, and N. Kutsevol**

*Chemical Department, Taras Shevchenko National University of Kyiv, City of Kyiv 01601, Ukraine*

Correspondence should be addressed to P. Virych; sphaenodon@ukr.net

Received 7 February 2020; Accepted 9 April 2020; Published 27 April 2020

Guest Editor: Juan Li



Cross-linked dextran-graft-polyacrylamide hydrogels with different cross-linking density loaded with methylene blue was prepared as light-activated antimicrobial materials. Sorption/desorption properties of hydrogels were studied by estimating the change in the absorption maximum of MB solutions. The sorption/desorption rate of MB into/out of hydrogel depends on the hydrogel structure. The antibacterial properties of the light-irradiated materials were tested against *Staphylococcus aureus*. It was shown that irradiation of hydrogels in the presence of methylene blue was able to eliminate the bacteria strains.

## 1. Introduction

Bacterial infection usually occurs in burns, wounds, and lots of surgical operations [1]. Microorganisms play an essential role in the development and maintenance of pathologies, and their removal during the wound healing or biomechanical preparation is important to the success of treatment. To eliminate or reduce bacterial colonization, methods that included the use of high-dose antibiotic were used. The antibiotic is largely successful but can lead to the development of antibiotic-resistant strains of bacteria. One novel approach for the elimination of bacteria on different surfaces is to use a light-activated antimicrobial agent (LAAA) [2, 3].

Light-activated antimicrobial agents when excited with light of an appropriate wavelength, namely, with red light, generate singlet oxygen and/or radicals which are highly cytotoxic to bacteria [4, 5]. The use of LAAAs to treat or prevent infectious diseases is known as photodynamic therapy (PDT) [6].

LAAAs are usually inorganic or organic dyes such as methylene blue (MB). LAAAs encapsulated in a polymer have shown to exhibit antimicrobial activity against a wide range of pathogenic bacteria [7–9]. The process used to encapsulate LAAAs into elastomers for medical application consisted of dipping the polymer into a LAAA solution containing a solvent capable of swelling the matrix; during this phase, the solution penetrates into the elastomer carrying the LAAA.

Hydrogels are water swellable materials having three-dimensional polymeric network possessing both the mechanical properties of solids and diffusive transport of liquids. They have microscopic pores and elasticity, which provide their water holding and swelling capacity. These properties made hydrogels promising materials for biomedical applications [10]. Recently, polysaccharide-based hydrogels have got attraction in drug delivery system and dressing materials due to their extraordinary swelling properties, biodegradability, biocompatibility, and nontoxicity [11].

In our recent studies, we reported a class of polyacrylamide hydrogels [12] obtained by cross-linking of star-like branched copolymers of PAA with polysaccharide. It was shown that dextran-graft-polyacrylamide (D20-PAA) hydrogels exhibited the advantages in comparison with hydrogels based on linear polyacrylamide. D20-PAA hydrogels can be designed to have optimal water or biological fluid content in aqueous medium, good mechanical properties, shape stability, and softness similar to that of the soft surrounding tissue. Considering the facts of using of hydrogels as wound dressing, in the present work, we attempt to create the hydrogel/MB composites and study the antimicrobial

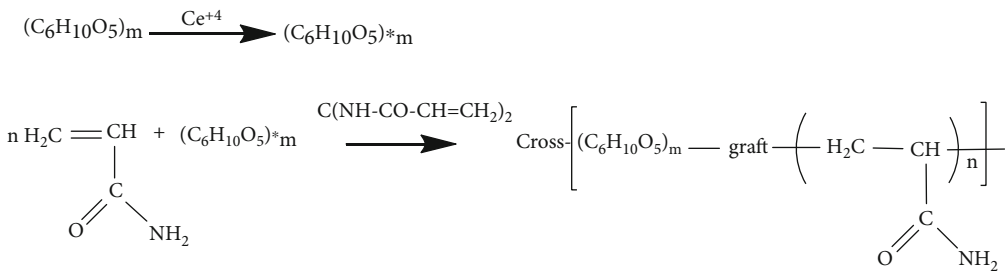


Figure 1: Schematic representation of hydrogel synthesis.

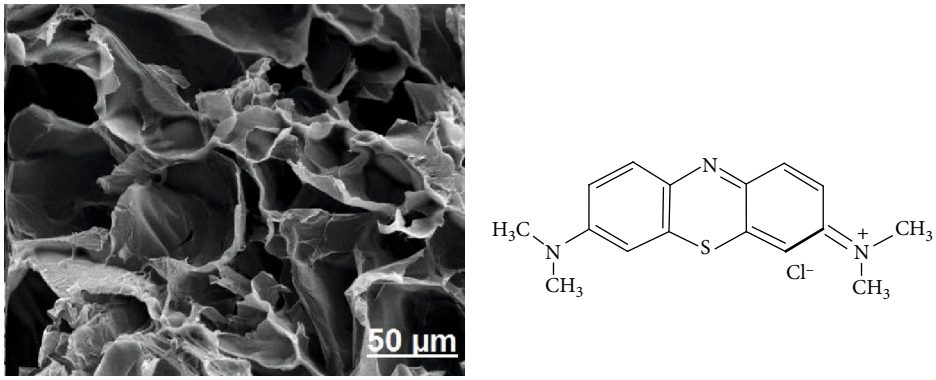


D20-PAA-x Methylene blue

Figure 2: Internal structure of cross-linked copolymer networks and chemical structure of dye.

photodynamic effect. The monochromatic visible light at $\lambda = 660$ nm was used due to its minimal negative effects on human tissues and ability to stimulate regeneration processes [13].

## 2. Materials and Methods

*2.1. Hydrogel Synthesis.* Dextran-graft-polyacrylamide (D20-PAA-x) hydrogels (Figure 1) with different concentrations of cross-linking agent ($x = 0.2$; 0.4 and 0.6 wt. %) were used. The synthesis of hydrogels is described in our previously work [12]. As precursors, we use acrylamide (AA) by Sigma-Aldrich. Dextran (D20) with $M_w = 20\,000$ g/mol, cerium (IV) ammonium nitrate (CAN), N,N′-methylene-bis-acrylamide (MBA), and methylene blue (MB) were purchased from Fluka. All supplied reagents were of analytical grade, and they were used without further purification. All procedures with hydrogels were performed in deionized water.

D20-g-PAA-x hydrogels were prepared by free radical polymerization using CAN as an initiator in the presence of cross-linking agent MBA [14] (Figure 1). The calculated amount of dextran (0.02 mM) was dissolved in 25 mL of distilled water at 25°C. This solution was purged by argon bubbling for 20 min, and then, initiator CAN (0.03 mmol) was added. In 2 min, AA (0.05 mol) and MBA (0.28, 0.4, or 0.6 g per 100 g of monomer AA) were poured into the reaction mixture. The formed hydrogel samples were taken out from the flask in 24 h, washed with distilled water to remove unreacted monomer. Finally, the gels were dried at ambient temperature.

*2.2. Determination of the Residual Acrylamide.* To control the amount of residual AA in hydrogels, high-performance liquid chromatography (HPLC) was used. Water extracts were analyzed by the Waters Alliance HPLC System with a diode-array detector. The column Nucleosil C18 (4 × 250 mm) was set at the temperature of 20°C. The detection was conducted at the wavelength of 210 nm. The mixture of methanol/redistilled water in the ratio 90/10 *v*/*v* was used as a mobile phase, at the flow rate of 1 mL $min^{-1}$. Calibration curves for determining the contents of AA were constructed by preparing a series of solutions with known concentrations.

*2.3. Preparation of Hydrogel Loaded with Methylene Blue.* Loading of methylene blue into hydrogels was carried out by saturation of swollen hydrogels from aqueous solutions of methylene blue. The dye concentrations were 0.0001 and 0.001 wt. %. Samples of 1 × 1 × 1 cm cubes (~1 g) of cured hydrogels were immersed in a solution of MB for 12 h. Internal structure of cross-linked copolymer networks and chemical structure of dye are shown in Figure 2.

*2.4. UV-Vis Spectroscopy.* The absorbance is measured using a Lambda 35 UV-Vis spectrophotometer (PerkinElmer, CA) in the absorbance mode (range 200–1000 nm), at the absorption maximum of the methylene blue ($\lambda_{max} = 668$ nm [15]). In this case, the greater the absorbance, the higher the dye concentration. The concentration of dye in solution did not exceed $0.25 \times 10^{-3}$ wt. %, to prevent dimerization of the dye and the appearance of an additional maximum of absorption.

Table 1: Diffusion rate of dye and equilibrium dye concentration at sorption of methylene blue by hydrogel.

| Sample | $V_1$* (min$^{-1}$) | $V_2$ (min$^{-1}$) | $C_{eq1} \times 10^4$ (wt. %) | $C_{eq2} \times 10^4$ (wt. %) |
|---|---|---|---|---|
| D20-PAA-0.2 | 0.10 | 0.40 | 4.16 | 1.46 |
| D20-PAA-0.4 | 0.08 | 0.35 | 3.64 | 1.59 |
| D20-PAA-0.6 | 0.07 | 0.33 | 2.94 | 1.61 |

*$V_1$ and $V_2$: diffusion rate of MB into hydrogel and out of hydrogel; $C_{eq1}$: equilibrium MB concentration in hydrogel at sorption; $C_{eq2}$: equilibrium MB concentration in solution at sorption.

All optical spectra were acquired using quartz cuvettes with a 1 cm path length.

*2.5. Dynamic Study of Dye Sorption and Desorption.* The dynamic study of dye diffusion into hydrogel (sorption) was carried out by estimating the change in the absorption maximum of MB solutions.

For this aim, the hydrogel sample of 7 mm in diameter was put into of aqueous solution of methylene blue ($C = 0.25 \times 10^{-3}$ wt. %). The mass ratio of hydrogels and solution in all experiments was 1 : 4. In 10 min, the absorbance of the solution of nonabsorbed dye was measured. Further measurements were carried out at time intervals of 10 min for 150 min until the equilibrium concentration of the dye in solution was reached. The concentration of the nonabsorbed dye was determined by the calibration curve, and the amount of dye absorbed by the hydrogel was concluded (Table 1).

The diffusion of methylene blue out of the saturated hydrogels was similarly studied. In this case, the hydrogel samples loaded with MB were put into distilled water. The mass ratio of loaded with MB hydrogels and water in all experiments was 1 : 4. The initial concentration of dye in all hydrogels was $0.25 \times 10^{-3}$ wt. %. In 10 min, the optical density of the solution of desorbed dye was measured. Further measurements were carried out at time intervals of 10 min for 150 min until the equilibrium concentration of the dye in solution was reached. The concentration of the desorbed dye was determined by the calibration curve.

To analyze the adsorption and desorption rate (V) of the dye, the first derivative of the dye concentration in solution vers time was calculated. For this purpose, the experimental dependence was linearized in logarithmic coordinates: time (ln $t$) vers absorbance (ln $D$) by fitting according to linear law; the slope of dependence obtained corresponds to the rate of dye diffusion. Slight deviations from the linear range do not exceed the permissible error of the experiment.

*2.6. Antibacterial Studies.* The LIKA-Led (Photonics Plus, Cherkasy, Ukraine) apparatus with laser emitters with wavelengths ($\lambda_{ex}$) of 660 nm was used. An irradiation with light from a 100 mW laser for up to 20, 30, and 40 min results in an energy density of 21 J/cm$^2$, 31.5 J/cm$^2$, and 42.1 J/cm$^2$, respectively.

The antimicrobial activity of methylene blue activated by red light was studied in a suspension of *S. aureus* ($10^5$ CFU/mL). A suspension of *S. aureus* ($10^{-5}$ CFU/mL) was prepared in a nonagar Müller-Hinton medium. 3.8 mL aliquots of the suspension were placed in tubes; then, 0.2 mL methylene blue solution of 0.02% wt. % was added into suspension and incubated at 37°C throughout the experiment. Both suspension of *S. aureus* and suspension of *S. aureus* with methylene blue were irradiated with light (660 nm) from a 100 mW laser for up to 3 min, resulting in an energy density of 0-18 J/cm$^3$. Each test was compared to the control because every 1-3 h, there was a multiplication of bacteria and a doubling of their number. The bactericidal effect was evaluated in % of CFU deaths relative to the control sample.

The antimicrobial activity of hydrogels loaded with methylene blue (0.0005 wt. %) in a suspension of *S. aureus* ($10^5$CFU/mL) was studied. The hydrogel samples were placed into bacteria suspension in a mass ratio of hydrogel: suspension = 1 : 4. After 120 min, the equilibrium concentration of MB in the solution was equal to 0.0001 ± 0.00002% wt. %. Further irradiation with light (660 nm, 100 mW) with interval of 20 min and an energy density of 6 J/cm$^3$ was carried out. The bactericidal effect was evaluated in % of CFU deaths relative to the control sample.

A disk diffusion method was applied to study the antibacterial activity of the hydrogels. Wild strains of *Staphylococcus aureus* were used as Gram-positive bacteria models in the test. Wild strains of bacteria were obtained on an electric medium "Yolk-salt agar" [16]. The sensitivity of the selected strains to the action of light and methylene blue was carried out on solid medium. A suspension of the bacteria (of approximately $10^5$ CFU/mL) was prepared to a particular standard, then spread evenly onto Müller-Hinton agar in a Petri dish.

The Petri dish was divided into four sectors hereinafter referred to as 1, 2, 3, and 4: for control (1), for irradiation with light (2), for hydrogel saturated with methylene blue (3), and for hydrogel saturated with methylene blue and irradiated with light (4). The hydrogel samples and their composites with MB were cut to 5 mm side squares and placed on Petri dishes with agar. Then, sector (2) and sector (4) were irradiated with light ($\lambda_{ex}$ = 660 nm). The agar plates were placed in an incubating oven at 37°C and left for 24 h.

The antimicrobial activity of MB-loaded hydrogels was assessed by analyzing the diameter of growth retardation [17]. Determination of colony-forming units (CFU) in bacterial suspensions was performed in the Goryaev chamber after staining an aliquot of the suspension with Acridine orange with a final dye concentration of 0.001 wt. % [18]. CFU was determined using luminescence Acridine orange at a wavelength of 530 nm.

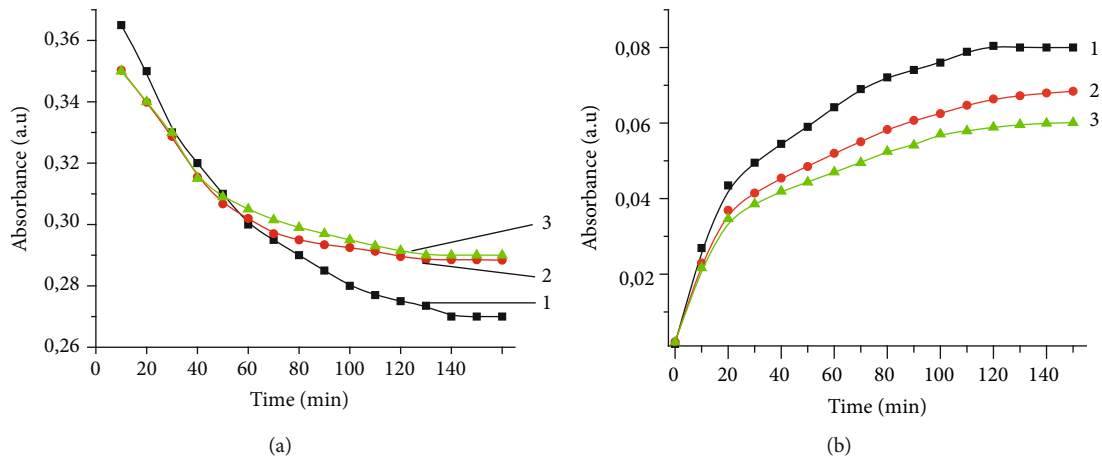


Figure 3: (a) The change in the absorption maximum of MB solution at $\lambda_{max}$ = 668 nm during dye diffusion in the hydrogel: 1: D20-PAA-0.2, 2: D20-PAA-0.4, and 3: D20-PAA-0.6; (b) the change in the absorption maximum of the methylene blue solution during dye diffusion from the hydrogel: 1: D20-PAA-0.2, 2: D20-PAA-0.4, and 3: D20-PAA-0.6.

All experiments were performed in triplicate, and mean average values were reported.

## 3. Results and Discussion

*3.1. Dynamic of Sorption/Desorption Studies.* The diffusion rate of methylene blue into hydrogel samples was studied by changing the in the absorption maximum of MB solution into which the hydrogel was placed. The decrease in the absorbance of the solution indicates a decrease in the concentration of dye and, thus, an increase in its concentration in the hydrogel (Figure 3(a)).

Figure 3(b) represents the diffusion of methylene blue out of the saturated hydrogels into water. In this case, the increase in the absorbance of dye in the solution at the absorbance maximum corresponds to an increase in its concentration in solution. The equilibrium state of the dye desorption from the hydrogel was reached in 130-150 min for all samples.

The concentration of MB in the hydrogel in the equilibrium state is represented in Table 1. It is evident that the degree of cross-linking of the hydrogel decreases and the rate of diffusion of methylene blue into the hydrogel increases. It is caused by higher mesh size as it was demonstrated in [12]. The equilibrium concentration of the dye in the hydrogel is higher than in the solution, which indicates the intermolecular interactions of the dye molecules and the polymer matrix due to polar functional groups and ionic interactions in local volume of hydrogel. The lower cross-linking density of hydrogels leads to higher concentration of dye into polymer matrices after diffusion.

Figure 3(b) shows the strong dependence of the diffusion process on the concentration of cross-links in the hydrogel. The release rate of loaded MB out of hydrogel is the highest for the sample D20-PAA-0.2 with the lowest cross-linking density, which corresponds to the largest mesh size in the network.

Thus, sorption/desorption properties of hydrogels are important factor for regulation of therapeutic concentrations of the active substances in bacteria medium. It allows creating novel materials for biomedical application, wound dressing, for example. So, we use hydrogels D20-PAA-0.2 with the best diffusion properties for antibacterial studies.

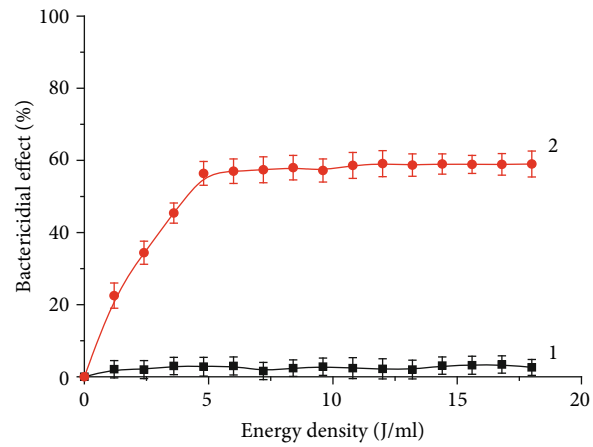


Figure 4: Bactericidal effect of red light (660 nm) (1) and methylene blue ($10^{-4}$ wt. %) activated by red light (660 nm) (2) in suspension of wild strains *S. aureus* (M ± SD).

*3.2. Antibacterial Studies*

*3.2.1. Antibacterial Activity of Light-Activated MB in the Bacterial Suspension.* The study of antibacterial efficacy of red light (660 nm) against *S. aureus* in the bacterial suspension indicates no bactericidal action (Figure 4). This is due to the low energy of light quanta and the absence of photosensitizer targets in bacterial cells. It was also found that methylene blue at a concentration of 0.0001 wt. % in the bacterial suspension does not show bactericidal properties relative to the bacterial strains. Then, red light irradiation and MB of 0.0001 wt. % were combined and caused 20% reduction in CFU with a small radiation dose of about 2 J/cm$^3$. An increase of energy density to 6 J/cm$^3$ causes to inactivate 60% of CFU. Further increase in the radiation dose does

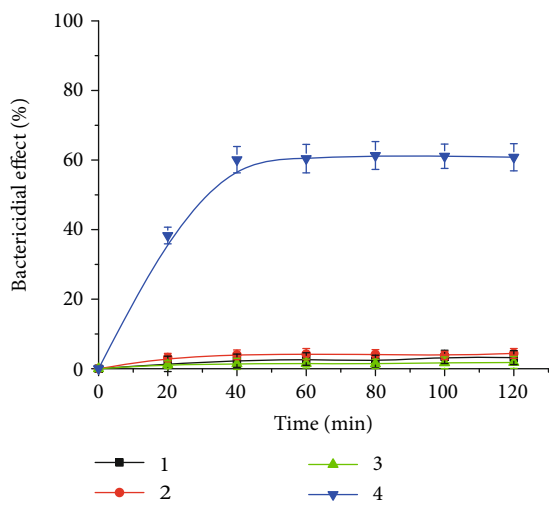


Figure 5: Bactericidal effect of red light (660 nm) (1), methylene blue ($10^{-4}$ wt.%) (2), pure D20-PAA-0.2 (3), and D20-PAA-0.2 loaded with MB and activated by red light (660 nm) (4) in suspension of wild strains *S. aureus*. Energy density = 6 J/cm$^3$, M ± SD.

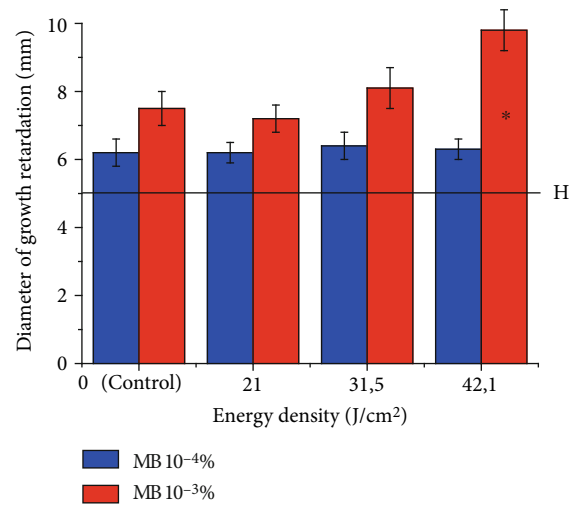


Figure 6: Bactericidal effect of D20-PAA-0.2 loaded with MB activated by red light (660 nm) on Müller-Hinton agar against wild strains *S. aureus*. $C_{MBA} = 10^{-3}$, $10^{-4}$ wt. %, H: diameter of the hydrogel sample, M ± SD, $^*p < 0.05$.

not contribute to the growth of bactericidal activity. This may be due to the adaptation of *S. aureus* culture to the conditions created or the lack of oxygen or dye in solution.

*3.2.2. Antibacterial Activity of Hydrogel Loaded with MB in the Bacterial Suspension.* The study of the diffusion of methylene blue out of the hydrogel into the solution has showed the gradual release of the dye into the environment in a short time. This allows for a long time to provide the required concentration of the active substance in the suspension of pathogenic bacteria. Considering obtained results, the bactericidal effect of hydrogel materials loaded with methylene blue in combination with visible light irradiation was investigated. D20-PA-0.2 of the lowest cross-linking density and the highest diffusion rate was separated as an MB container. First of all, it was shown that individual components such as pure hydrogel, light irradiation at 6 J/cm$^3$, and methylene blue do not possess antibacterial ability in bacterial suspension (Figure 5). At the same time, complex action of hydrogel composite D20-PAA-0.2/MB and light irradiation resulted in loss of 60% of the initial amount of CFU, with the incubation of the hydrogel in a solution of 40 min.

*3.2.3. Antibacterial Activity of Hydrogels Loaded with MB on Solid Medium.* The described above results of antibacterial studies in bacterial suspension indicate the antibacterial efficacy of composites based on cross-linked hydrogels loaded with methylene blue and activated by red light irradiation. Since such composites are promising materials for hydrogel dressings, it was interesting to study their antibacterial properties on the surface. Antibacterial efficacy is known to be caused by several factors such as the nature of the light-activated antimicrobial agent, their diffusion rate and concentration, hydrogel nature, and bacteria strains.

The bactericidal activity of hydrogels D20-PAA-0.2 loaded with MB at low concentrations of $1 \times 10^{-3}$ and $1 \times 10^{-4}$ wt. % against wild *Staphylococcus aureus* strains was investigated by the disc-diffusion method (Figure 6). As seen from Figure 6, irradiation of hydrogel loaded with MB at $1 \times 10^{-4}$ wt. % with different light energy density (660 nm) does not lead the appreciable bactericidal activity. When increasing the concentration of MB to$1 \times 10^{-3}$ wt. %, its bactericidal activity increases and its dependence on radiation doses appears.

Thus, the hydrogel composites loaded with methylene blue as light-activated antimicrobial agent and irradiated with red light (660 nm) possess bactericidal effect both in suppressive and in solid media. It makes them promising materials for wound dressings and application for photodynamic therapy.

## 4. Conclusions

Hybrid cross-linked hydrogel dextran-grafted-polyacrylamide with different cross-linking density was synthesized as promising materials of a new generation for biomedical application. Methylene blue was used as the universal model of light-activated antimicrobial agent. Sorption/desorption process of dye into/out of hydrogels was studied. The release rate of absorbed MB into hydrogel was higher for the sample with the lowest cross-linking density. Antibacterial activity of hydrogel composites loaded with methylene blue as light-activated antimicrobial agent and irradiated with red light was tested in suspension and solid medium against wild strains *S. aureus*. The high antimicrobial efficacy was registered for both experiments. Thus, prepared hydrogel composites can be used as promising materials for wound dressings and photodynamic therapy.

## Data Availability

The [Dynamic of sorption/desorption studies] data used to support the findings of this study are included within the article. The [Antibacterial studies] data used to support the findings of this study are available from the corresponding author upon request.

## Conflicts of Interest

The authors declare that there is no conflict of interest regarding the publication of this paper.

## References

[1] W. Kim, W. Zhu, G. L. Hendricks et al., "A new class of synthetic retinoid antibiotics effective against bacterial persisters," *Nature*, vol. 556, no. 7699, pp. 103–107, 2018.

[2] P. S. Zolfaghari, S. Packer, M. Singer et al., "In vivo killing of Staphylococcus aureus using a light-activated antimicrobial agent," *BMC Microbiology*, vol. 9, no. 1, p. 27, 2009.

[3] M. Wilson, T. Burns, and J. Pratten, "Killing of Streptococcus sanguis in biofilms using a light-activated antimicrobial agent," *Journal of Antimicrobial Chemotherapy*, vol. 37, no. 2, pp. 377–381, 1996.

[4] K. Page, M. Wilson, and I. P. Parkin, "Antimicrobial surfaces and their potential in reducing the role of the inanimate environment in the incidence of hospital-acquired infections," *Journal of Materials Chemistry*, vol. 19, no. 23, pp. 3819–3831, 2009.

[5] V. Decraene, J. Pratten, and M. Wilson, "Cellulose acetate containing toluidine blue and rose bengal is an effective antimicrobial coating when exposed to white light," *Applied and Environmental Microbiology*, vol. 72, no. 6, pp. 4436–4439, 2006.

[6] R. A. Hsi, D. I. Rosenthal, and E. Glatstein, "Photodynamic therapy in the treatment of cancer," *Drugs*, vol. 57, no. 5, pp. 725–734, 1999.

[7] S. Perni, P. Prokopovich, C. Piccirillo, J. Pratten, I. P. Parkin, and M. Wilson, "Toluidine blue-containing polymers exhibit potent bactericidal activity when irradiated with red laser light," *Journal of Materials Chemistry*, vol. 19, no. 18, pp. 2715–2723, 2009.

[8] J. Gil-Tomás, S. Tubby, I. P. Parkin et al., "Lethal photosensitisation of *Staphylococcus aureus* using a toluidine blue O-tiopronin-gold nanoparticle conjugate," *Journal of Materials Chemistry*, vol. 17, no. 35, pp. 3739–3746, 2007.

[9] K. Edwards, "New twist on an old favorite: gentian violet and methylene blue antibacterial foams," *Advances in Wound Care*, vol. 5, no. 1, pp. 11–18, 2016.

[10] Q. Chai, Y. Jiao, and X. Yu, "Hydrogels for biomedical applications: their characteristics and the mechanisms behind them," *Gels*, vol. 3, no. 1, p. 6, 2017.

[11] R. Parhi, "Cross-linked hydrogel for pharmaceutical applications: a review," *Advanced Pharmaceutical Bulletin*, vol. 7, no. 4, pp. 515–530, 2017.

[12] O. Nadtoka, N. Kutsevol, A. Naumenko, and P. Virych, "Photochemical synthesis and characterization of hydrogel–silver nanoparticle composites," *Research on Chemical Intermediates*, vol. 45, no. 8, pp. 4069–4080, 2019.

[13] Y. Wang, Y. Y. Huang, Y. Wang, P. Lyu, and M. R. Hamblin, "Red (660 nm) or near-infrared (810 nm) photobiomodulation stimulates, while blue (415 nm), green (540 nm) light inhibits proliferation in human adipose- derived stem cells," *Scientific Reports*, vol. 7, no. 1, article 7781, 2017.

[14] O. Nadtoka, N. Kutsevol, V. Krysa, and B. Krysa, "Hybrid polyacryamide hydrogels: synthesis, properties and prospects of application," *Molecular Crystals and Liquid Crystals*, vol. 672, no. 1, pp. 1–10, 2018.

[15] S. Perni, C. Piccirillo, A. Kafizas et al., "Antibacterial activity of light-activated silicone containing methylene blue and gold nanoparticles of different sizes," *Journal of Cluster Science*, vol. 21, no. 3, pp. 427–438, 2010.

[16] L. M. Carantonis and M. S. Spink, "A selective salt egg agar medium for pathogenic staphylococci," *The Journal of Pathology*, vol. 86, no. 1, pp. 217–220, 1963.

[17] M. Lehtopolku, P. Kotilainen, P. Puukka et al., "Inaccuracy of the disk diffusion method compared with the agar dilution method for susceptibility testing of Campylobacter spp," *Journal of Clinical Microbiology*, vol. 50, no. 1, pp. 52–56, 2012.

[18] C. Camacho-Fernández, D. Hervás, A. Rivas-Sendra, M. P. Marín, and J. M. Seguí-Simarro, "Comparison of six different methods to calculate cell densities," *Plant Methods*, vol. 14, no. 1, p. 30, 2018.

Hindawi
International Journal of Polymer Science
Volume 2020, Article ID 8109294, 8 pages
https://doi.org/10.1155/2020/8109294

*Research Article*

# Isoflurane Regulates Proliferation, Apoptosis, and Inflammatory Response of Lipopolysaccharide-Induced Human Astrocyte through the miR-206/BDNF Axis

**Jianying Wang, Zhiyuan Liu, Xue Wang, and Yu Liu**

*Yiwu Central Hospital, Yiwu, 322000 Zhejiang, China*

Correspondence should be addressed to Yu Liu; ycwyly@yeah.net

Received 31 December 2019; Accepted 14 March 2020; Published 26 March 2020

Guest Editor: Can Yang Zhang



*Objective*. To investigate the effect of isoflurane (ISO) on the proliferation, apoptosis, and inflammatory response of lipopolysaccharide- (LPS-) induced normal human astrocytes (NHAs) by regulating the miR-206/BDNF axis. *Methods*. NHA proliferation activity was measured by MTT; NHA apoptotic rates were measured by Annexin V-FITC/PI; western blotting was used to measure the BDNF expression; ELISA was used to measure the IL-6, IL-1$\beta$, and TNF-$\alpha$ expression in NHAs; qPCR was used to measure the expressions of miRNAs that are related to NHAs proliferation and apoptosis; dual-luciferase reporter was constructed to validate the targeting relationship between miR-206 and BDNF. *Results*. LPS increased the proliferation activity and decreased the apoptosis rate of NHAs which were effectively reversed by the ISO ($p < 0.05$); LPS significantly inhibited the expression of miRNAs related to proliferation and apoptosis in NHAs ($p < 0.05$, $p < 0.01$), whereas ISO significantly increased the expression of miR-206 ($p < 0.01$) by downregulating the expression of BDNF, thus inhibiting NHA proliferation and inflammatory response and enhancing apoptosis. *Conclusion*. ISO can inhibit the expression of BDNF by upregulating the expression of miR-206, thereby inhibiting the proliferation and inflammatory response of NHAs and promoting its apoptosis.

## 1. Introduction

Recently, the incidence of neurodegenerative diseases such as amyotrophic lateral sclerosis (ALS) and spinal cord injury (SCI) is increasing, and the central nervous system inflammatory response is a potential mechanism for various neurodegenerative diseases [1]. It has been reported that the normal human astrocytes (NHAs) can minimize primary damage and repair damaged tissues. However, under certain pathological conditions, NHAs can change to become reactive NHAs [2], and reactive NHAs are one of the main sources of proinflammatory cytokines in the brain [3]. NHAs are involved in the development of a variety of neurodegenerative diseases [4]; therefore, studying the mechanism of reactive NHAs is helpful for the development of protective strategies for neurodegenerative diseases induced by central nervous system inflammation. Lipopolysaccharide (LPS) is the main component of Gram-negative endotoxin [5], and it is an effective immune system-activating factor, which is usually used to study inflammation-related diseases [6]. Therefore, in this study, LPS was used to treat NHAs to establish an in vitro LPS-induced NHA injury model. Isoflurane (ISO) is a commonly used inhalation anesthetic and has been shown to have neuroprotective effects by inhibiting inflammatory responses [7], but its regulatory effect on reactive NHAs has not been reported. It has been demonstrated that miR-206 was able to inhibit the inflammatory response to reduce neural pain [8] and also to regulate the proliferation and apoptosis of nerve cells [9], but the effect on NHA cells is unknown. A bioinformatics study suggests that brain-derived neurotrophic factor (BDNF) is a target protein of miR-206 and has been proved to be an important target for the treatment of neurodegenerative diseases [10]. Therefore, this study aimed at investigating the effects

of ISO on the proliferation, apoptosis, and inflammatory response of NPS cells induced by lipopolysaccharide through the miR-206/BDNF axis.

## 2. Materials and Methods

*2.1. Cell Lines and Reagents.* NHAs (Cat. No. 1800) were purchased from Shanghai Fumeng Gene Biotechnology Co., Ltd. The DMEM complete medium, penicillin, streptomycin, fetal bovine serum, Lipofectamine 2000 transfection reagent, one-step reverse transcription kit, TRIzol kit, and dual-luciferase reporter gene kit were purchased from Thermo Fisher. The Annexin V-FITC/PI Apoptosis Detection Kit was purchased from Biotech Bioengineering (Shanghai) Co., Ltd. The ELISA kit was purchased from Shanghai Gaining Biotechnology Co., Ltd. RIPA cell lysates were purchased from Beijing Solaibao Technology Co., Ltd. LPS was purchased from Shanghai Guchen Biotechnology Co., Ltd. Isoflurane was purchased from Jinan Huifengda Chemical Co., Ltd. BDNF primary and secondary antibodies were purchased from Wuhan Aimeijie Technology Co., Ltd.

*2.2. Cell Culture.* NHAs were cultured and incubated in the DMEM medium containing 10% fetal bovine serum, 1% penicillin, and streptomycin and cultured in a 37°C, 5% $CO_2$ incubator. The culture medium was replaced every day. The passage was performed at a confluency of 70 to 80%, and cells from passages 3 to 4 were used for subsequent experiments.

*Drug treatment*. NHAs in logarithmic growth phase were taken and treated with different concentrations of LPS (0 $\mu$g/mL, 0.2 $\mu$g/mL, 0.5 $\mu$g/mL, and 1 $\mu$g/mL) for 24 h, and the appropriated LPS concentration was selected. After 24 h of treatment with LPS (0.5 $\mu$g/mL), the NHAs were placed in a closed anesthesia box. The inlet end was connected to an ISO gas volatilizer, and 95% air and 5% $CO_2$ were passed in. The outlet end was connected to an anesthetic gas monitor for the ISO concentration examination. Different concentrations of ISO (0.7%, 1.4%, and 2.1%) were passed in for 2 h, and then cell proliferation, apoptosis, and inflammatory factors were measured.

*2.3. Cell Transfection.* NHAs in the logarithmic growth phase were taken, inoculated into 6-well plates, and cultured in a 37°C, 5% $CO_2$ incubator. When the confluence of the cells reaches 70~80%, miR-206 mimics, anti-miR-206, NC-mimics, and si-BDNF were transfected into NHAs and cultured in a 5% $CO_2$ incubator at 37°C for 48 h before use.

*2.4. NHA Proliferation Activity Measured by MTT.* Each group of NHAs to be tested in the logarithmic growth phase was taken and inoculated in a 96-well plate at a density of $1 \times 10^4$ cells/well. 10 $\mu$L MTT solution was subsequently added when the cells cultured for 0, 24, 48, 72, and 96 h. After a further 4 h of incubation, the culture supernatant was aspirated, and 100 $\mu$L of dimethyl sulfoxide (DMSO) was added; finally, the absorbance (OD) was measured at 450 nm using a microplate reader.

*2.5. NHA Apoptotic Rates Detected by Annexin V-FITC/PI Double Staining.* NHAs to be tested in each group were collected and cultured for 48 h and digested with 0.25% trypsin and centrifuged at 1000 r/min for 5 min. After that, the cells were adjusted to a concentration of $5 \times 10^5$ cells/mL, and 5 $\mu$L Annexin V-FITC was added and mixed well. After homogenization, the cells were incubated at room temperature for 15 min in the dark, then 5 $\mu$L of PI staining solution was added, mixed, and incubated for 5 min; and finally, flow cytometry was used to detect the apoptosis level of NHAs.

Table 1: qPCR primer sequences.

| Primer | Sequence (5′-3′); F: forward primer, R: reversed primer |
|---|---|
| miR-211 | F: 5′-TTGTGGGCTTCCCTTTGTCATCCT-3′ |
| | R: 5′-TGCTGTGGGAAGTGACAACTGA-3′ |
| miR-146a | F: 5′-CCTGAGAAGTGAATTCCATGGG-3′ |
| | R: 5′-TGGTGTCGTGGAGTCG-3′ |
| miR-140 | F: 5′-CCCAAGCTTTTTCCGTGGTGACCTCCTCT-3′ |
| | R: 5′-CGCGGATCCTGCTGGGCTGTTTGTGGGGG-3′ |
| miR-206 | F: 5′-CGGGCTTGTGGAATGGTAAGC-3′ |
| | R: 5′-GCTTCGGCAGCACATATACTAAAAT-3′ |
| U6 | F: 5′-CTCGCTTCGGCAGCACA-3′ |
| | R: 5′-AACGCTTCACGAATTTGCGT-3′ |

*2.6. Expression of IL-6, IL-1β, and TNF-α in NHAs Determined by ELISA.* Each group of NHAs to be tested was collected and prepared into a cell suspension, and the expression of IL-6, IL-1$\beta$, and TNF-$\alpha$ in NHAs was determined according to the corresponding ELISA kit instructions.

*2.7. miRNAs Expression in NHAs Measured by qPCR.* The TRIzol method was used to extract the total RNA, which was then reverse transcribed into cDNA according to the instructions of the miRNA reverse transcription kit. qPCR was used according to the instructions on the miRNA qPCR kit. U6 was used as an internal reference, and the primer sequences are shown in Table 1. The relative expressions were calculated using $2^{-\Delta\Delta Ct}$.

*2.8. BDNF Expression in NHAs Detected by Western Blotting.* NHAs of each group in the logarithmic growth phase were taken and washed twice with PBS. A total of 0.5 $\mu$g/mL LPS were added to the experimental group, and cells were rinsed with PBS twice after 24 h of culture. After that, 1 mL of PBS was added before centrifugation (3000 r/min) for 5 min. After centrifugation, the supernatant was discarded, and the cells were washed three times by adding icy PBS before the addition of the RIPA lysis buffer. The BCA protein quantification kit was used to determine the protein concentration. An equal amount of protein samples was then taken from each group for the SDS-PAGE electrophoresis. After electrophoresis, the SDS-PAGE gel was transferred to a PVDF membrane and placed in a 5% skim milk powder for blockage for 1.5 h. A primary antibody (1 : 1000) was added and incubated at 4°C overnight. On the next day, after washing the membrane once with TBST, an HRP-labeled secondary

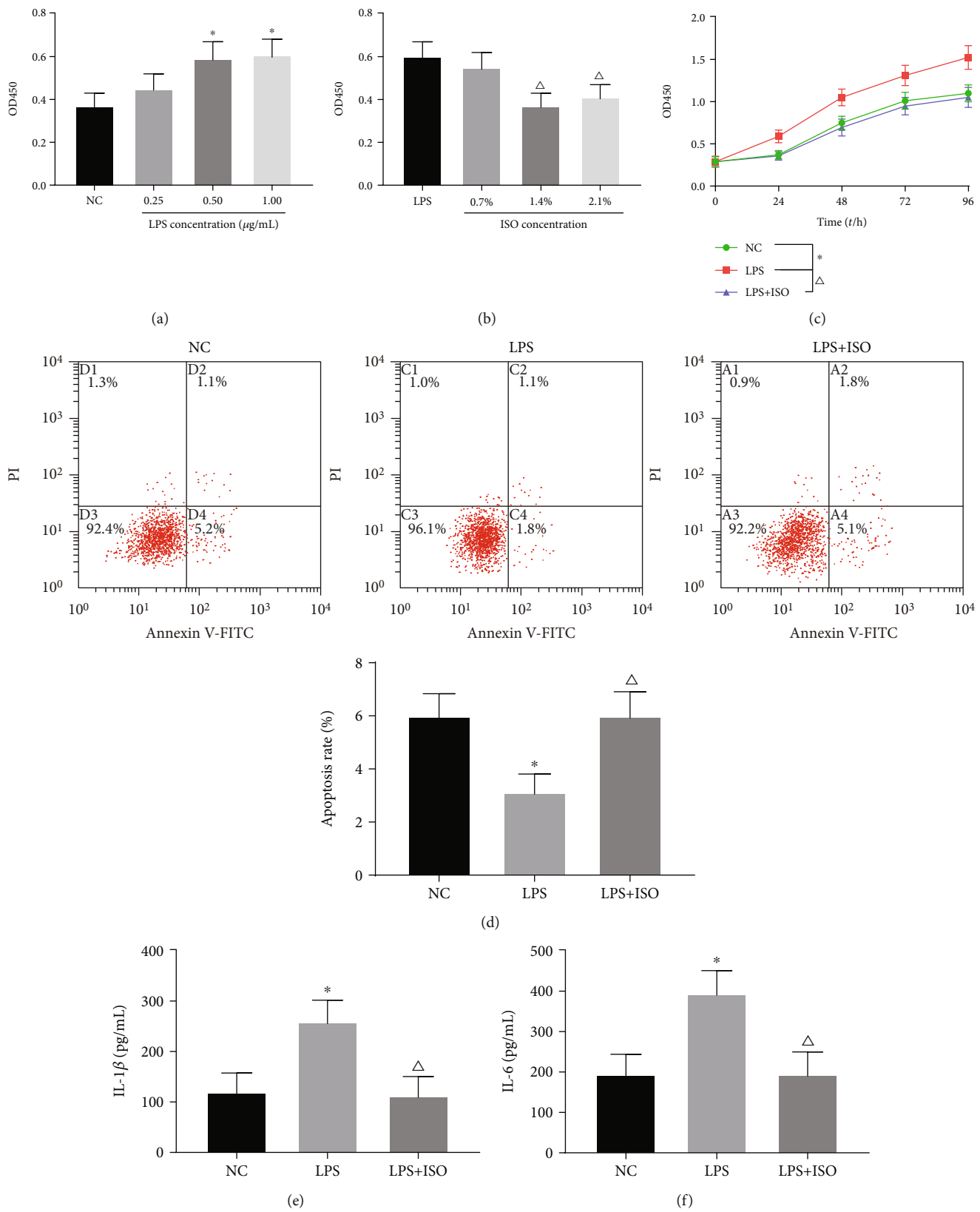


Figure 1: Continued.

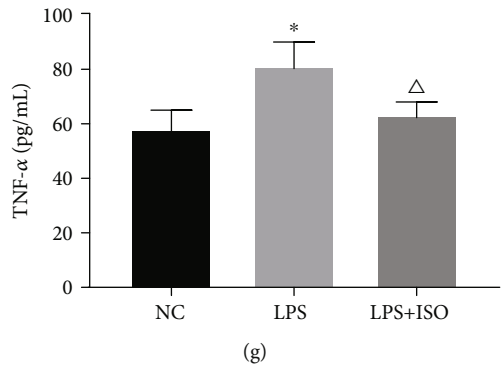


Figure 1: Effects of ISO on LPS-induced NHAs proliferation, apoptosis, and inflammatory response. $^{*}p < 0.05$ vs. the *NC* group; $^{\Delta}p < 0.05$ vs. the *LPS* group. (a–c) The proliferation of NHAs measured by MTT. (d) NHA apoptosis measured by Annexin V-FITC/PI. (e–g) Expression of IL-6, IL-1$\beta$, and TNF-$\alpha$ in NHAs determined by ELISA.

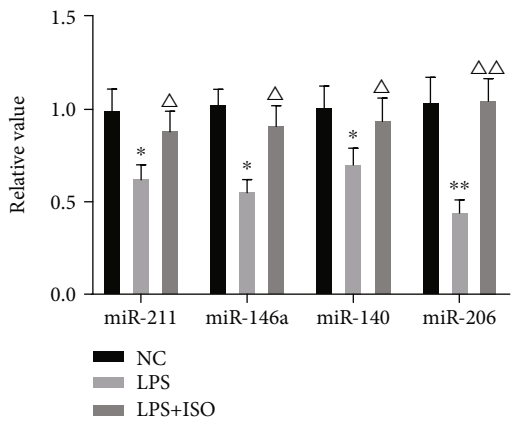


Figure 2: ISO upregulated the expression of miR-206 in NHAs cells. $^{*}p < 0.05$, $^{**}p < 0.01$ vs. the *NC* group; $^{\Delta}p < 0.05$, $^{\Delta\Delta}p < 0.01$ vs. the *LPS* group.

antibody (1 : 5000) was added to the sample and incubated for 1.5 h at room temperature. After that, the membrane was washed three times with TBST, and the ECL kit was used for the development of the protein bands. The ImageJ software was then used to analyze the grayscale of the bands and calculate the relative expression.

*2.9. Targeting the Relationship between miR-206 and BDNF Verified by Dual-Luciferase Reporter.* The StarBase database was used to predict the binding site of miR-206 and BDNF. The BDNF wild-type vector (WT-BDNF) was constructed; gene mutation technology was used to change the binding site of miR-206 and BDNF, and the BDNF mutant vector (MUT-BDNF) was constructed by the same method. WT-BDNF or MUT-BDNF was then cotransfected with miR-206 mimics or miR-NC into NHAs and cultured for 48 h, and the luciferase activity of each group was measured using the dual-luciferase reporter gene kit [8].

*2.10. Statistical Analysis.* All experiments in this study were repeated three times, and data were expressed as $\bar{x} \pm s$. The GraphPad 7.0 software was used for statistical analysis and related figure drawing. *t*-test was used for comparison between two groups, and one-way analysis of variance was used for comparison between multiple groups. $p < 0.05$ and $p < 0.01$ were used to indicate a statistically significant difference.

## 3. Results

*3.1. Effect of ISO on LPS-Induced NHAs Proliferation, Apoptosis, and Inflammatory Response.* MTT results showed that the cell proliferation ability increased in a dose-dependent manner after treatment of NHAs with different concentrations of LPS (0.0 $\mu$g/mL, 0.2 $\mu$g/mL, 0.5 $\mu$g/mL, and 1.0 $\mu$g/mL) (Figure 1(a), $p < 0.01$), and there is no significant difference in cell proliferation activity when LPS was at a concentration of 0.5 $\mu$g/mL and 1 $\mu$g/mL. After NHAs were first treated with 0.5 $\mu$g/mL LPS, different concentrations of ISO (0.7%, 1.4%, and 2.1%) were introduced, and the proliferation activity of NHAs was found to be the lowest at 1.4% after 2 h (Figure 1(b), $p < 0.01$). MTT, Annexin V-FITC/PI, and ELISA were used to measure the proliferation activity, apoptosis rate, IL-6, IL-1$\beta$, and TNF-$\alpha$ expression of NHAs in the NC group, LPS group, and LPS+ISO group. The results showed that compared with the NC group, the proliferation activity and the expression of IL-6, IL-1$\beta$, and TNF-$\alpha$ were significantly increased, and the apoptosis rate was significantly reduced in the LPS group, whereas the LPS+ISO group reversed the effects of the LPS on NHA proliferation, apoptosis, and inflammatory response (Figures 1(c)–1(e), all $p < 0.05$). Therefore, taken together, ISO can reverse the promotion effect of LPS on the proliferation and inflammatory response of NHAs and the inhibitory effect on apoptosis.

*3.2. ISO Upregulated miR-206 Expression in NHAs.* qPCR results showed that LPS significantly inhibited the expression of miRNAs [2, 11–13] associated with proliferation and apoptosis of NHAs ($p < 0.05$, $p < 0.01$), and the addition of ISO reversed these inhibitory effects to a certain extent. In particular, among all examined miRNAs, miR-206 was the most significantly reversed one (Figure 2, $p < 0.01$). Therefore, it can be concluded that ISO upregulated the expression of miR-206 in NHAs.

*3.3. miR-206 Downregulated BDNF.* The bioinformatics database StarBase was used to predict that BDNF is a potential

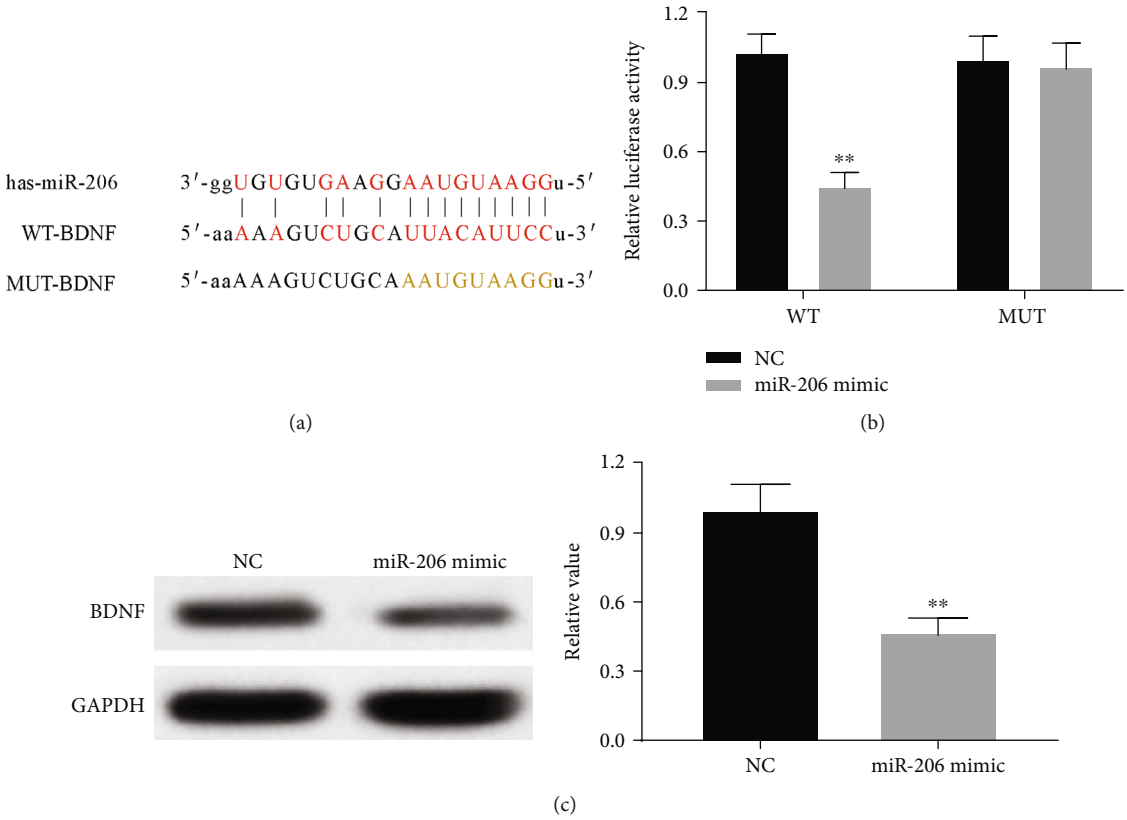


Figure 3: miR-206 targeted downregulation of BDNF. (a) The bioinformatics analysis result showed that BDNF was a target gene of miR-206. (b) The dual-luciferase reporter gene assay was used to verify the relationship between miR-206 and BDNF. (c) Western blotting was applied to measure the expression of BDNF. $^{**}p < 0.01$ vs. the *NC* group.

target gene for miR-206 (Figure 3(a)). The results of the dual-luciferase reporter gene showed that the overexpression of miR-206 significantly reduced the luciferase activity of the WT-BDNF plasmid ($p < 0.01$); however, it had no significant effect on the luciferase activity of the MUT-BDNF plasmid ($p > 0.05$). Western blotting results (Figure 3(c)) also confirmed that the overexpression of miR-206 significantly inhibited BDNF expression in NHAs ($p < 0.01$). These results suggested that miR-206 targeted and downregulated BDNF expression.

*3.4. ISO Regulated the LPS-Induced Proliferation, Apoptosis, and Inflammatory Response of NHAs via the miR-206/BDNF Axis.* Western blotting was used to detect BDNF expression in NHAs after treatment with LPS, and the results showed that after knocking down BDNF, BDNF expression in NHAs was significantly reduced ($p < 0.01$); in addition, after simultaneous knockdown of BDNF and miR-206, BDNF expression was significantly increased compared with knockdown of BDNF alone ($p < 0.01$), and there was no significant difference compared with the NC group. After NHAs were treated with LPS, MTT, Annexin V-FITC/PI, and ELISA were used to detect the proliferation activity, apoptosis rate, and IL-6 IL-1$\beta$ expression of NHAs in NC group, ISO group, ISO +anti-miR-206 group, ISO+si-BDNF group, and ISO+anti-miR-206+si-BDNF group. The results showed that compared with the NC group, the proliferation activity, IL-6, IL-1$\beta$, and TNF-$\alpha$ expression of NHAs in ISO group were significantly reduced, while the apoptosis rate increased significantly, whereas addition of anti-miR-206 effectively reversed the effects of the ISO on NHAs proliferation, apoptosis, and inflammatory response. However, in the ISO+si-BDNF group, the effects of the ISO group on NHAs proliferation, apoptosis, and inflammatory responses were further heightened. Compared with the ISO+anti-miR-206 group, the proliferation activity and inflammatory response of NHAs cells in the ISO+anti-miR-206+si-BDNF group were reduced, while the apoptosis rate was increased.

Compared with the ISO+si-BDNF group, the proliferation activity and inflammatory response of NHAs in the ISO+anti-miR-206+si-BDNF group increased, whereas the apoptosis rate decreased as shown in Figures 4(b)–4(d) (all $p < 0.05$). Taken all these together, it seems that ISO can reverse the effects of LPS on NHAs including the promotion of proliferation, inflammatory response, and inhibition of apoptosis by regulating the miR-206/BDNF axis.

## 4. Discussion

Normal human NHAs are the most abundant cell types in the central nervous system, providing nutritional support for neurons and maintaining the function of the central nervous system [14]. Studies have shown that the function of NHAs is regulated by microglia, microorganisms, and

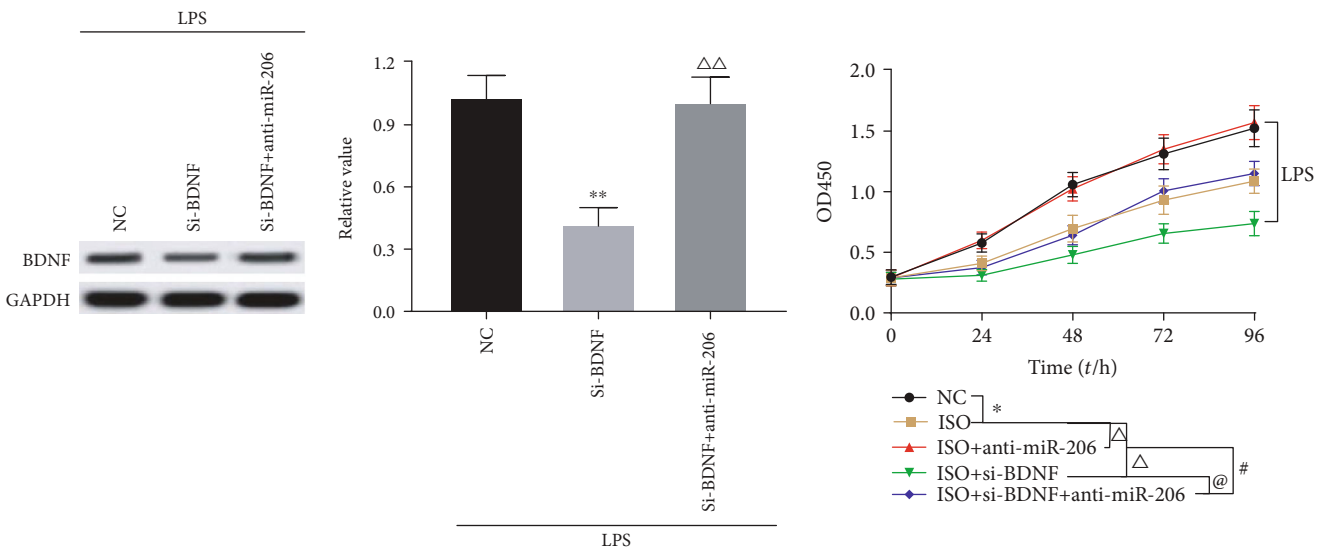


(a) (b)

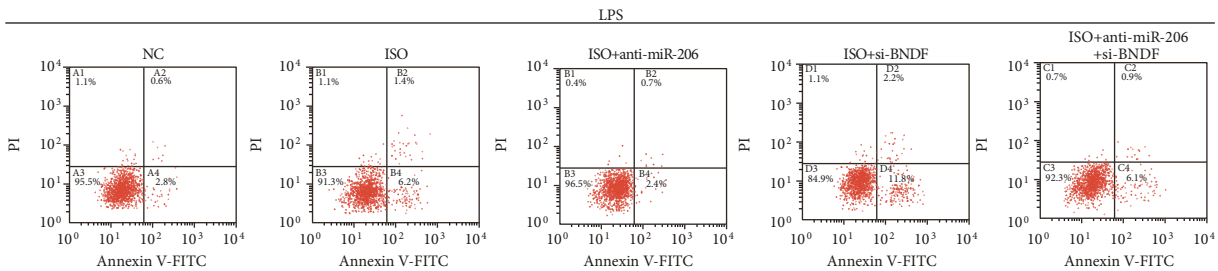


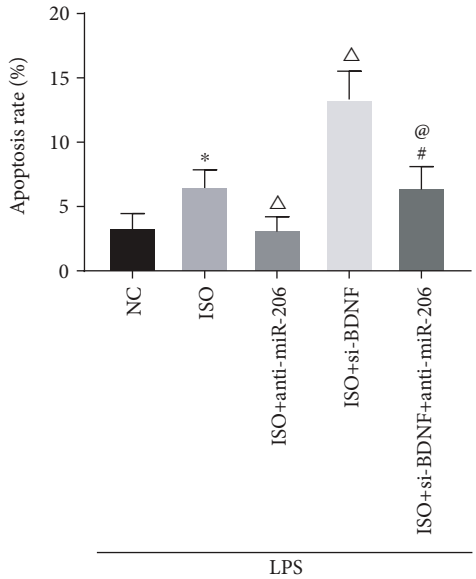


(c)

Figure 4: Continued.

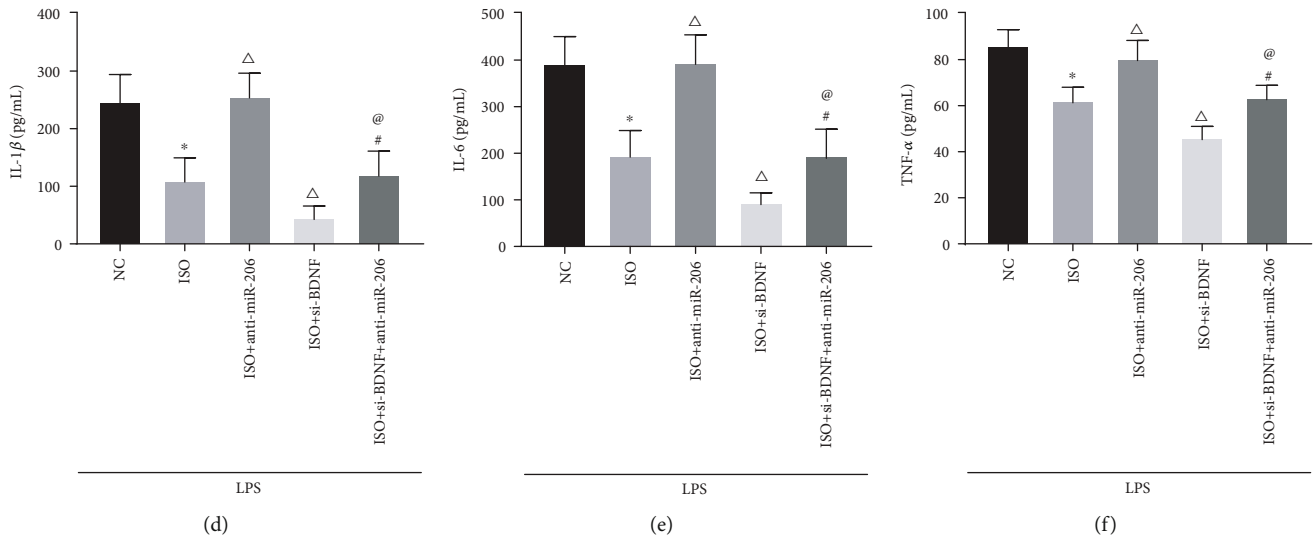


Figure 4: ISO regulated the effects of miR-206/BDNF axis on LPS-induced NHA cell proliferation, apoptosis, and inflammatory response. (a) Western blotting was applied to measure the expression of BDNF. (b) The proliferation activity of NHAs cells was detected by MTT. (c) Annexin V-FITC/PI was used to detect NHA cell apoptosis. (d–f) Expression of IL-6, IL-1$\beta$, and TNF-$\alpha$ in NHAs cells was detected by ELISA. $^{*}p < 0.05$ vs. the *NC* group; $^{\Delta}p < 0.05$ vs. the *ISO* group; $^{\#}p < 0.05$ vs. the *ISO+anti-miR-206*; $^{@}p < 0.05$ vs. the *ISO+si-BDNF*.

the internal environment [15], and under the stimulation of the inflammatory environment, NHAs can lose most of the normal astrocyte functions and gain new neurotoxic function [16]. It has also been reported that NHA cell-derived inflammation is a common component of acute or chronic damage to the central nervous system [17] and plays a key regulatory role in the pathogenesis of various neurodegeneration caused by neuroinflammation [18]. The results in our study found that LPS can promote the proliferation and inflammatory response of NHA cells and inhibit its apoptosis.

ISO is a commonly used inhalation anesthetic and is widely used in various types of surgery to maintain general anesthesia. In addition, ISO also has anti-inflammatory, antioxidant, and apoptotic effects [1]. It has been reported that ISO can regulate immune and inflammatory responses by reducing neutrophil function and inhibiting cytokines release by macrophages and attenuating the response of natural killer cells to interferon-$\alpha$4, finally to exert anti-inflammatory effects by reducing systemic inflammation and inhibiting cytokines release by mononuclear cells and macrophages release [19]. Moreover, studies have demonstrated that ISO was able to protect brain damage. For instance, Swissa [7] and others found that ISO significantly reduced the late-stage brain damage in the rat model of epilepsy status induced by oxophosphate. However, it has not yet been reported whether ISO regulates reactive NHA cell-derived inflammation. Our results discovered that ISO can inhibit LPS-induced proliferation and inflammatory response and promote apoptosis of NHAs cells.

miR-206 has been shown associated with neuronal activation and neuroinflammation [20] and is abnormally lowly expressed in the serum of chronic neuropathy rats [21]. In addition, miR-206 can regulate inflammatory responses. For example, overexpression of miR-206 can reduce neuropathic pain caused by overexpression of ZEB2 in microglia in rats by inhibiting neuroinflammation [22]. BDNF is produced and secreted by neurons, it can promote the development of axons in an autocrine manner, and it is essential in the development of brain circuits [3]. In addition, BDNF, as a neurotrophic protein, plays an important role in the plasticity of the central nervous system and is also involved in the pathogenesis of neurological diseases [23], thus becoming an important target for the treatment of neurodegenerative diseases. The results in this study illustrated that ISO can upregulate miR-206 expression, and miR-206 can inhibit LPS-induced glial cell proliferation, inflammatory, and promote its apoptosis through downregulation of BDNF expression.

In summary, ISO can reduce the inflammatory response under pathological conditions by upregulating the inhibitory effect of miR-206, inhibiting LPS-induced NHAs proliferation, and enhancing apoptosis.

## Data Availability

All the data is available with the handwritten notebook documented in our lab.

## Conflicts of Interest

The authors declare that there are no conflicts of interest regarding the publication of this paper.

## Acknowledgments

This work is supported by the Zhejiang Science and Technology Department Project (No. 2013C33216).

## References


[1] S. Yang, J. Liu, X. Zhang et al., "Anesthetic isoflurane attenuates activated microglial cytokine-induced VSC4.1 motoneuronal apoptosis," *American Journal of Translational Research*, vol. 8, no. 3, pp. 1437–1446, 2016.

[2] K. Zhang, S. Wu, Z. Li, and J. Zhou, "MicroRNA-211/BDNF axis regulates LPS-induced proliferation of normal human astrocyte through PI3K/AKT pathway," *Bioscience Reports*, vol. 37, no. 4, 2017.

[3] T. Tanaka, S. Kai, T. Matsuyama, T. Adachi, K. Fukuda, and K. Hirota, "General anesthetics inhibit LPS-induced IL-1beta expression in glial cells," *PLoS One*, vol. 8, no. 12, article e82930, 2013.

[4] A. Birger, I. Ben-Dor, M. Ottolenghi et al., "Human iPSC-derived astrocytes from ALS patients with mutated C9ORF72 show increased oxidative stress and neurotoxicity," *EBioMedicine*, vol. 50, pp. 274–289, 2019.

[5] Y. Ding, J. Zhang, and R. Wang, "Inhibition of tissue transglutaminase attenuates lipopolysaccharide-induced inflammation in glial cells through AKT/mTOR signal pathway," *Biomedicine & Pharmacotherapy*, vol. 89, pp. 1310–1319, 2017.

[6] X. Tao, M. Yan, L. Wang et al., "Homeostasis imbalance of microglia and astrocytes leads to alteration in the metabolites of the kynurenine pathway in LPS-induced depressive-like mice," *International Journal of Molecular Sciences*, vol. 21, no. 4, p. 1460, 2020.

[7] E. Swissa, G. Bar-Klein, Y. Serlin et al., "Midazolam and isoflurane combination reduces late brain damage in the paraoxon-induced status epilepticus rat model," *Neurotoxicology*, vol. 78, pp. 99–105, 2020.

[8] W. Sun, L. Zhang, and R. Li, "Overexpression of miR-206 ameliorates chronic constriction injury-induced neuropathic pain in rats via the MEK/ERK pathway by targeting brain-derived neurotrophic factor," *Neuroscience Letters*, vol. 646, pp. 68–74, 2017.

[9] R. Wang, Y. Hu, G. Song et al., "MiR-206 regulates neural cell proliferation and apoptosis via Otx2," *Cellular Physiology and Biochemistry*, vol. 29, no. 3-4, pp. 381–390, 2012.

[10] C. Deng, J. Zhu, J. Yuan, Y. Xiang, and L. Dai, "Pramipexole inhibits MPP (+)-induced neurotoxicity by miR-494-3p/BDNF," *Neurochemical Research*, vol. 45, no. 2, pp. 268–277, 2019.

[11] J. Mei, R. Bachoo, and C. L. Zhang, "MicroRNA-146a inhibits glioma development by targeting Notch1," *Molecular and Cellular Biology*, vol. 31, no. 17, pp. 3584–3592, 2011.

[12] Z. Tu, Y. Li, Y. Dai et al., "MiR-140/BDNF axis regulates normal human astrocyte proliferation and LPS-induced IL-6 and TNF-alpha secretion," *Biomedicine & Pharmacotherapy*, vol. 91, pp. 899–905, 2017.

[13] T. J. Liu, B. Wang, Q. X. Li, X. L. Dong, X. L. Han, and S. B. Zhang, "Effects of microRNA-206 and its target gene IGF-1 on sevoflurane-induced activation of hippocampal astrocytes in aged rats through the PI3K/AKT/CREB signaling pathway," *Journal of Cellular Physiology*, vol. 233, no. 5, pp. 4294–4306, 2018.

[14] L. Udovin, C. Quarracino, M. I. Herrera, F. Capani, M. Otero-Losada, and S. Perez-Lloret, "Role of Astrocytic Dysfunction in the Pathogenesis of Parkinson's Disease Animal Models from a Molecular Signaling Perspective," *Neural Plasticity*, vol. 2020, Article ID 1859431, 10 pages, 2020.

[15] M. A. Wheeler, I. C. Clark, E. C. Tjon et al., "MAFG-driven astrocytes promote CNS inflammation," *Nature*, vol. 578, no. 7796, pp. 593–599, 2020.

[16] S. A. Liddelow, K. A. Guttenplan, L. E. Clarke et al., "Neurotoxic reactive astrocytes are induced by activated microglia," *Nature*, vol. 541, no. 7638, pp. 481–487, 2017.

[17] X. Duan, A. Zohaib, Y. Li et al., "miR-206 modulates lipopolysaccharide-mediated inflammatory cytokine production in human astrocytes," *Cellular Signalling*, vol. 27, no. 1, pp. 61–68, 2015.

[18] A. Montoya, D. Elgueta, J. Campos et al., "Dopamine receptor D3 signalling in astrocytes promotes neuroinflammation," *Journal of Neuroinflammation*, vol. 16, no. 1, p. 258, 2019.

[19] X. Guo, J. Deng, B. Zheng et al., "HDAC1 and HDAC2 regulate anti-inflammatory effects of anesthetic isoflurane in human monocytes," *Immunology and Cell Biology*, 2020.

[20] M. Kashyap, S. Pore, M. Chancellor, N. Yoshimura, and P. Tyagi, "Bladder overactivity involves overexpression of MicroRNA 132 and nerve growth factor," *Life Sciences*, vol. 167, pp. 98–104, 2016.

[21] Y. Xu, X. Zhang, S. Pu, J. Wu, Y. Lv, and D. du, "Circulating microRNA expression profile: a novel potential predictor for chronic nervous lesions," *Acta Biochimica et Biophysica Sinica*, vol. 46, no. 11, pp. 942–949, 2014.

[22] Z. L. Chen, J. Y. Liu, F. Wang, and X. Jing, "Suppression of MALAT1 ameliorates chronic constriction injury-induced neuropathic pain in rats via modulating miR-206 and ZEB2," *Journal of Cellular Physiology*, vol. 234, no. 9, pp. 15647–15653, 2019.

[23] G. Cavaliere, G. Trinchese, E. Penna et al., "High-fat diet induces neuroinflammation and mitochondrial impairment in mice cerebral cortex and synaptic fraction," *Frontiers in Cellular Neuroscience*, vol. 13, p. 509, 2019.

Hindawi
International Journal of Polymer Science
Volume 2020, Article ID 2391439, 9 pages
https://doi.org/10.1155/2020/2391439

*Research Article*

# *Cyclocarya paliurus* Polysaccharide Inhibits Glioma Cell U251 Proliferation, Migration, and Invasion and Promotes Apoptosis via the GSK3$\beta$/$\beta$-Catenin Signaling Pathway

**Xiaolong Du, Kai Guo, Yongqian Ma, and Jianyong Chang**

*Department of Neurosurgery, Weifang People's Hospital, Weifang, Shandong, China 261000*

Correspondence should be addressed to Jianyong Chang; changjy82@126.com

Received 23 December 2019; Revised 2 February 2020; Accepted 27 February 2020; Published 17 March 2020

Guest Editor: Can Yang Zhang



*Objective*. To investigate the effects of *Cyclocarya paliurus* polysaccharide (CPP) on the proliferation, migration, invasion, and apoptosis of human glioma U251 cells and further explore the underlying mechanism. *Methods*. U251 cells were cultured in vitro and treated with various concentrations (25, 50, 75, 100, 125, and 150 $\mu$mol/L) of CPP for 24, 48, and 72 h. Cell counting kit-8 was used to detect the activity of cell proliferation. Wound-healing assay, Transwell assay, and flow cytometry were used to measure the effects of CPP on the migration, invasion, and apoptosis of U251 cells, respectively. Western blotting was used to determine the protein expression involved in the GSK3$\beta$/$\beta$-catenin signaling pathway and its downstream genes related to proliferation, migration, invasion, and apoptosis including Cyr61, CCND1, Vimentin, and Slug. Meanwhile, qRT-PCR was used to detect the mRNA levels of Cyr61, CCND1, Vimentin, and Slug. *Results*. We found that CPP not only could inhibit the proliferation, migration, and invasion of U251 cells but also promote its apoptosis in vitro. Besides, CPP could significantly inhibit the phosphorylation and decrease the protein levels of GSK3 $\beta$ at ser9 site ($p < 0.05$), and thus increasing the phosphorylation of $\beta$-Catenin at ser33/37 site ($p < 0.05$), resulting in $\beta$-Catenin degradation. In addition, we also found that CPP could downregulate the mRNA ($p < 0.05$) and protein expression ($p < 0.05$) of downstream genes of GSK3 $\beta$/$\beta$-catenin signaling pathway including Cyr61, CCND1, Vimentin, and Slug, which are related to proliferation, migration, invasion, and apoptosis. *Conclusion*. CPP could inhibit the expression of GSK3$\beta$, promote the degradation of $\beta$-catenin, and downregulate the levels of GSK3$\beta$/$\beta$-catenin downstream genes including Cyr61, CCND1, Vimentin, and Slug, which regulate the proliferation, migration, invasion, and apoptosis of glioma cells.

## 1. Introduction

Glioma is one of the most aggressive malignant brain cancers, accounting for approximately 36% of primary brain tumors [1]. Glioma originates from glial cells and accounts for about 80% of malignant tumors of the central nervous system [2]. Although gliomas have a lower incidence than other cancers, gliomas have a relatively high mortality rate due to their highly invasive growth characteristics [3]. At present, despite the advances in treatment over the past decade, there is still no effective cure [4]. Chemotherapy is an important method for the treatment of gliomas. It can kill residual tumors that cannot be removed by surgery and radiotherapy. Therefore, it is of great significance to research the antiglioma drugs.

*Cyclocarya paliurus* is a plant of the genus *Chrysanthemum* (Jugaceae), mainly distributed in southern China. Its branches and leaves are sweet, having a cooling effect, and can reduce swelling and pain [5]. Modern pharmacological studies have shown that *Cyclocarya paliurus* contains a variety of nutrients and can play different biological roles [6]. Among these bioactive ingredients, *Cyclocarya paliurus* polysaccharide (CPP) is an important active ingredient. CPP and its complexes play critical roles in antitumor, anti-inflammatory, antiviral, antiaging, and anticoagulation [7–11]. Recent researches on CPP have mainly focused on its anticancer

effect. For instance, Jin et al. reported that the combination of CPP and X-rays had significant proliferation inhibition and proapoptotic effects on SW480 colorectal cancer cells [12]; Zhang et al. found that CPP could increase the sensitivity of hypoxic A549 and H520 human non-small-cell lung cancer cells to radiotherapy. These studies show the potential of CPP as a chemotherapeutic agent for clinical tumor treatment [13]. However, there is currently no article on the role of CPP in gliomas, so this study will use the glioma cell line U251 for the first time to study the role of CPP in cell proliferation, migration, and invasion.

## 2. Material and Methods

*2.1. Extraction and Identification of CPP.* Crude polysaccharides were extracted from the leaves of *Cyclocarya paliurus* by water extraction and alcohol precipitation method, deproteinized by Sevag method, and dried by water dialysis. After that, the crude polysaccharide was purified using a D301R column and eluted with the 0.4 m aqueous solution of sodium chloride [11]. The extracted CPP was identified by the ultraviolet spectrum and infrared spectrum.

*2.2. Determination of Molecular Weight and Analysis of Monosaccharide Components.* The molecular weight of CPP was determined by high-performance liquid chromatography (1100, Agilent, USA). The system was equipped with SHODEX KS-802 and KS-804 columns (7.8 mm × 300 mm), and a refractive index detector was used and the sample input was 20 $\mu$L. The sample was eluted with a NaCl aqueous solution (0.2 m) as a mobile phase at a flow rate of 0.8 ml/min, and the column temperature was maintained at 40°C. A series of standard dextran with known molecular weight values was used as the calibration curve, and the molecular weight was analyzed by Agilent-GPC software. A qq7000 capillary column (30 m × 0.25 mm × 0.25 m, Agilent, USA) and a hydrogen ionized flame detector (FID) were used in the gas chromatography analysis of monosaccharides in CPP. Specifically, the dried CPP (2.0 mg) was dissolved in 1.0 ml TFA (2.0 M), hydrolyzed in an ampule at 120°C for 90 min, washed with methanol, and then evaporated to remove TFA. The hydrolysate was reduced with NaBH4 and acetylated with ethyl acetate at 100°C for 60 min, and then, the acetic anhydride was destroyed with ice water. The obtained alditol was extracted with chloroform, and the resultant was analyzed by gas chromatography. The gas chromatography analysis procedure was as follows: injection temperature: 250°C; detector temperature: 250°C; column temperature increased from 120°C to 250°C, with an increasing rate of 3°C/min, and finally maintained at 250°C for 5 minutes. Nitrogen was used as the carrier gas and maintained at 1 mL/min. Air and hydrogen velocities were 400 and 30 mL/min, respectively. Seven monosaccharides were used as reference materials to quantitatively determine the monosaccharide content of CPP.

*2.3. Cell Culture.* Human glioma cells U251 were purchased from ATCC, USA. U251 cells were routinely cultured using DMEM medium (Thermo Fisher Scientific Inc., China) containing 10% fetal bovine serum (Gibco, USA), 100 U/mL penicillin, and 100 g/mL streptomycin (Gibco, USA). The temperature of the humidified incubator was maintained at 37°C and contained 5% carbon dioxide. Experiments were performed using only cells in the exponential growth phase.

*2.4. Cell Counting Kit-8 (CCK-8) Detects Cell Proliferation Activity.* U251 cells were seeded at a density of $5 \times 10^3$ cells/well in a 96-well plate and cultured overnight. The next day, CPP of different concentrations (25, 50, 75, 100, 125, and 150 $\mu$mol/L) prepared with cell culture medium [14] was added. For the control group, 10 $\mu$L CCK-8 reagent (Dojindo, Japan) was added per well at 24, 48, and 72 h. After a certain period of incubation, the absorbance ($A$) at 450 nm was measured on a spectrophotometer. The relative cell activity (%) is calculated as relative cell activity (%) = ($A$ (experimental group) − $A$ (blank group))/($A$ (control group) − $A$ (blank group)).

*2.5. Cell Scratch Test to Assess Cell Migration Ability.* U251 cells were seeded in a 12-well plate and cultured overnight. The next day, cells were treated with CPP at different concentrations and cultured until the cell fusion rate reached 95%. A sterile 100 $\mu$L pipette tip was used to draw a straight line on the monolayer cells, then the cells were washed with PBS. After that, 1% FBS DMEM medium and different concentrations of CPP were added. 24 h later, the cells that migrated to the injured area were observed and photographed under an inverted microscope.

*2.6. Cell Invasion Assay to Detect Cell Invasion.* For the cell invasion test, the upper chamber of the Transwell chamber (Corning, USA) was coated with a mixture containing 100 $\mu$L of Matrigel (Corning, USA) and serum-free DMEM medium. After the Matrigel coagulated, cells with certain density were seeded into the upper chamber of DMEM without FBS, and at the same time, DMEM medium containing 10% fetal bovine serum was added to the lower chamber. After 24 h incubation at 37°C, the invading cells were fixed with 20% methanol and stained with 0.1% crystal violet. The cells were photographed and counted under a microscope.

*2.7. Detection of Apoptosis by Flow Cytometry.* U251 cells were seeded in 6-well plates and incubated overnight. The next day, each well was added with different concentrations of CPP and cultured in an incubator for 72 h. The cells were collected, centrifuged, and washed according to the instructions of the flow cytometry kit (Biyuntian, China). 5 $\mu$L of Annexin V (fluorescein isothiocyanate) was added to the cell suspension and incubated for 15 minutes under the light. 10 $\mu$L of propidium iodide (PI) was added for double staining and incubated for 5 minutes in the dark. The analysis was performed within 1 h after the incubation.

*2.8. Western Blotting Method to Determine Cell Protein Expression Level.* After the cells were extracted with RIPA strong lysate (Biyuntian, China), the protein was quantified by the BCA method. 50 $\mu$g of the protein sample was loaded on the 10% SDS-PAGE electrophoresis gel, and Western blotting was carried out on a PVDF membrane (Invitrogen,

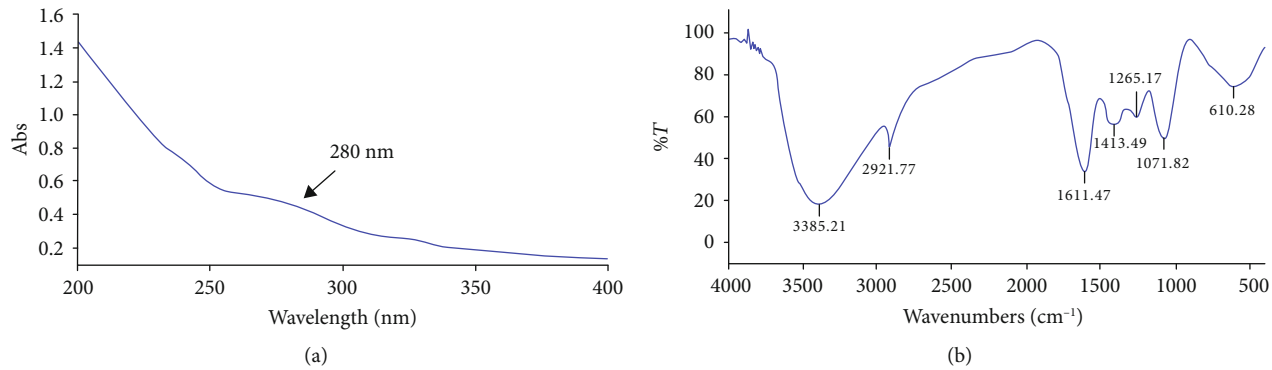


Figure 1: Identification of CPP in polysaccharides. (a) Ultraviolet spectrum identification result of CPP; (b) infrared spectrum identification result of CPP.

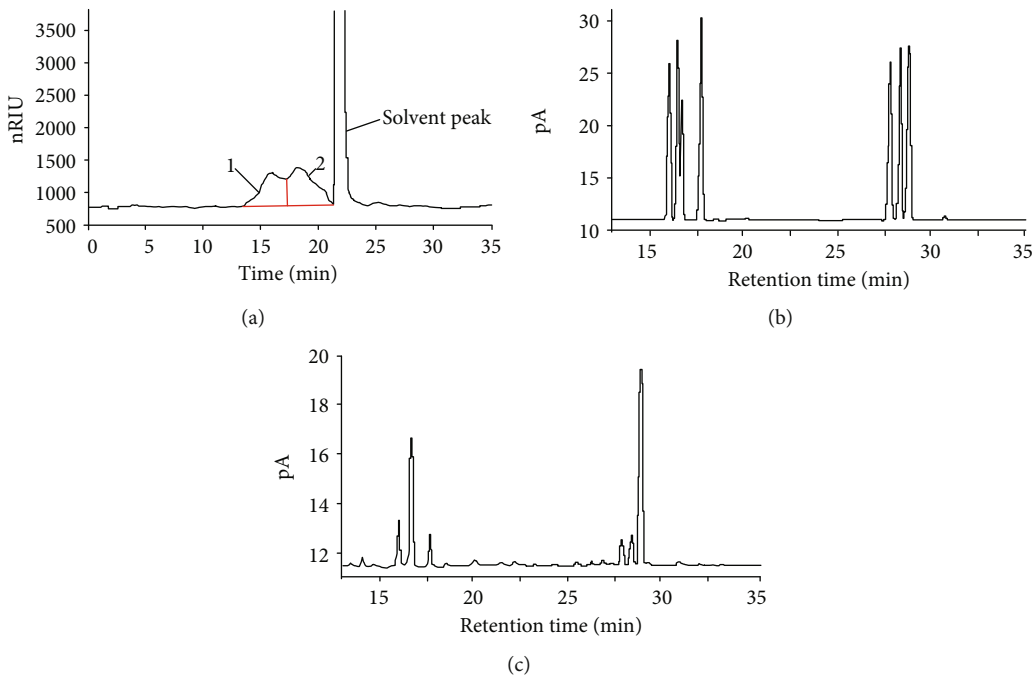


Figure 2: Molecular weight and gas chromatography analysis of CPP. (a) High-performance liquid chromatogram, (b) gas chromatogram of monosaccharide standard, and (c) gas chromatogram of CPP monosaccharide.

USA). The membrane was blocked at room temperature, washed with TBST after blocking, and primary antibody reaction solution including p-GSK3$\beta$ (Ser9, ab131097, Abcam, USA), GSK3$\beta$ (ab93926, Abcam, USA), p-$\beta$-catenin (Ser33/37, Ab11350, Abcam, UK), $\beta$-catenin (ab16051, Abcam, USA), Cyr61 (ab24448, Abcam, USA), CCDN1 (ab134175, Abcam, USA), Vimentin (ab8978, Abcam, USA), Slug (ab51772, Abcam, USA), and $\beta$-actin (ab179467, Abcam, USA) was added and incubated overnight at 4°C. The corresponding HRP-conjugated secondary antibody was added and incubated at room temperature after TBST elution. The image was then developed on the ECL luminescence imaging system.

*2.9. Detection of mRNA Expression by Real-Time Fluorescent Quantitative PCR (qPCR).* Total cellular RNA was extracted using TRIzol reagent (Invitrogen, USA). RNA concentration and purity were then measured spectrophotometrically and reversely transcribed (Takara, Japan) into cDNA. SYBR Green PCR Master Mix (Takara, Japan) was used for PCR amplification (Applied Biosystems, USA), $\beta$-actin was used as the housekeeping gene, and the relative expression of Cyr61, CCND1, Vimentin, and Slug mRNA was calculated using the $2^{-\Delta\Delta Ct}$ method. Experiments were repeated 3 times independently.

The primer sequences are as follows: Cyr61 preprimer (5′-3′): AGCAGCCTGAAAAAGGGCAA, postprimer (5′-3′): AGCCTGTAGAAGGGAAACGC; CCND1 preprimer (5′-3′): GCTGCGAAGTGGAAACCATC, postprimer (5′-3′): CCTCCTTCTGCACACATTTGAA; Vimentin preprimer (5′-3′): GACGCCATCAACACCGAGTT, postprimer (5′-3′): CTTTGTCGTTGGTTAGCTGGT; Slug preprimer (5′

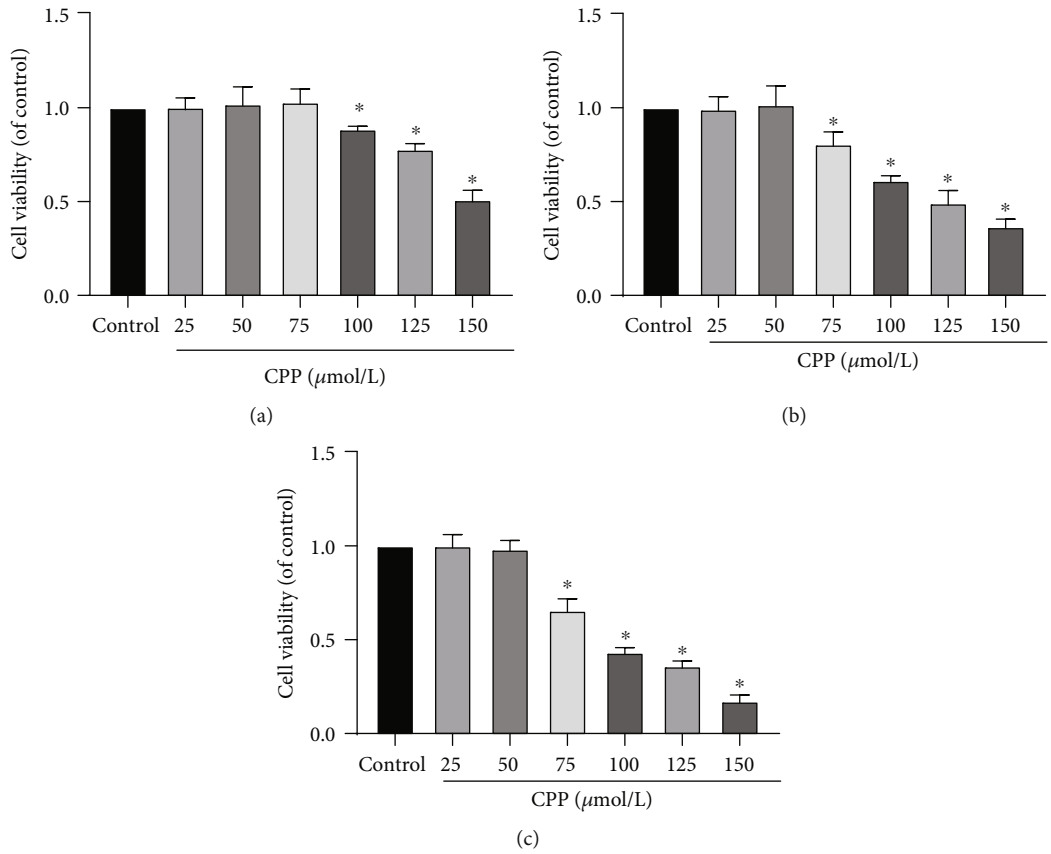


Figure 3: CPP inhibits U251 cell viability. (a–c) Changes in cell viability after 24, 48, and 72 h of CPP treatment (25, 50, 75, 100, 125, and 150 $\mu$mol/L) at different concentrations. Compared with the control group, $*$ indicates $p < 0.05$. This experiment was repeated three times independently.

-3′): CGAACTGGACACACATACAGTG, postprimer (5′-3′): CTGAGGATCTCTGGTTGTGGT; and $\beta$-actin preprimer (5′-3′): CATGTACGTTGCTATCCAGGC, postprimer (5′-3′): CTCCTTAATGTCACGCACGAT.

*2.10. Statistical Analysis.* Experimental data were expressed as mean ± standard deviation. Statistical analysis was performed using SPSS 18.0 software. Student's $t$-test was used for pairwise comparison of data between groups, and univariate analysis of variance was used for comparison within groups. $p < 0.05$ was considered statistically significant.

## 3. Results

*3.1. Isolation, Purification, and Structural Analysis of CPP.* As shown in Figure 1(a), CPP had no absorption at 260 nm, which indicates that there was no nucleic acid. The weak peak height at 280 nm was due to the presence of the protein, but whether the protein was a free protein or a dextran protein complex was not clear. The total sugar content of CPP determined by the phenol-sulfuric acid method was 62.4%. As shown in the infrared spectrum of Figure 1(b), the broad peak at 3385.21 $cm^{-1}$ and the weak absorption peak at 2921.77 $cm^{-1}$ were due to the C—H stretching of the CH2 group. The strong absorption peak at 1611.47 $cm^{-1}$ was due to the C=O asymmetric tensile vibration of the carboxylic acid group and wide absorption peaks at 1413.49 $cm^{-1}$ were caused by the deformation vibration of hydrogen bonds. The three bands at 3400, 2922, and 1414 $cm^{-1}$ were characteristic of polysaccharides. The C—O—C asymmetric tensile vibration band appeared at about 1265.17 $cm^{-1}$, and the symmetrical tensile vibration appears at about 1071.82 $cm^{-1}$.

Table 1: U251 cell viability changes under different concentrations and time of CPP treatment.

| Groups | 24 h | 48 h | 72 h |
|---|---|---|---|
| Control | 1 | 1 | 1 |
| CPP 25 $\mu$mol/L | 1.00 ± 0.05 | 0.99 ± 0.07 | 1.00 ± 0.06 |
| CPP 50 $\mu$mol/L | 1.02 ± 0.09 | 1.02 ± 0.10 | 0.98 ± 0.05 |
| CPP 75 $\mu$mol/L | 1.03 ± 0.07 | 0.81 ± 0.07 | 0.66 ± 0.06 |
| CPP 100 $\mu$mol/L | 0.89 ± 0.02 | 0.61 ± 0.03 | 0.43 ± 0.03 |
| CPP 125 $\mu$mol/L | 0.78 ± 0.03 | 0.49 ± 0.07 | 0.36 ± 0.03 |
| CPP 150 $\mu$mol/L | 0.51 ± 0.05 | 0.37 ± 0.04 | 0.17 ± 0.03 |

Note: compared with the control group, $^*p < 0.05$.

As shown in Figure 2(a), CPP was mainly divided into two parts, namely, CPP-1 and CPP-2. The average molecular weight (Mw) of CPP-1 was $1.32 \times 10^5$, the number average

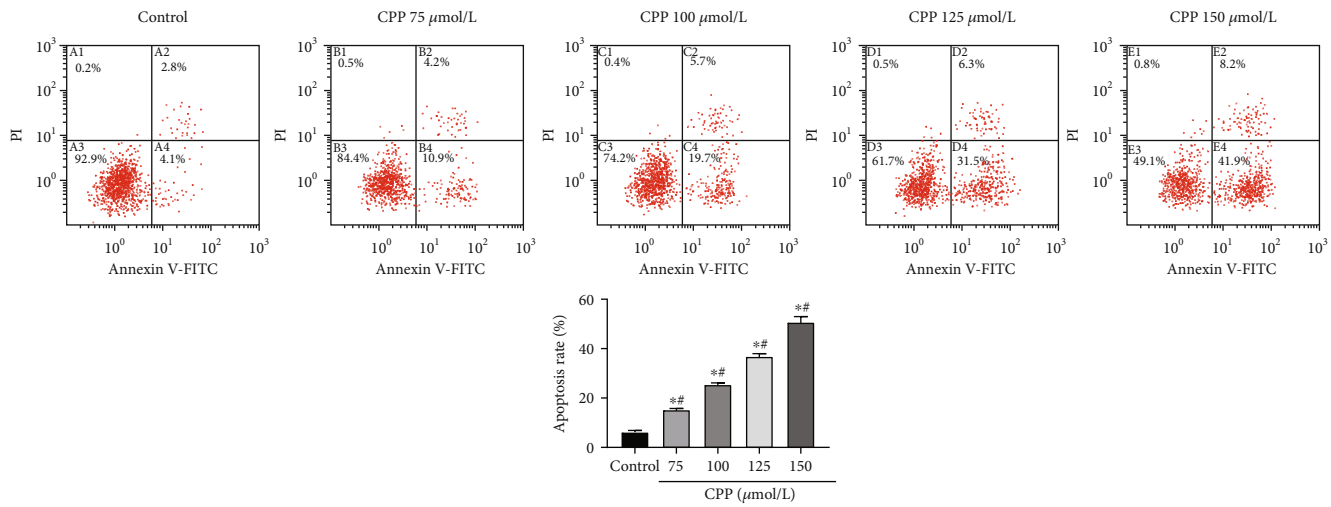


Figure 4: CPP induces apoptosis of U251 cells. Compared with the control group, ∗ indicates $p < 0.05$. Comparison between treatment groups with different concentrations of CPP (75, 100, 125, and 150 μmol/L), # indicates $p < 0.05$. This experiment was repeated three times independently.

molecular weight (Mn) was $9.83 \times 10^4$, the $Z$ average molecular weight (Mz) was $1.97 \times 10^5$, the Mw of CPP-2 was $9.31 \times 10^3$, the Mn was $5.41 \times 10^3$, and the Mz was $1.34 \times 10^4$. As shown in Figures 2(b) and 2(c), the following monosaccharides were separated by gas chromatography: rhamnose, fucose, arabinose, xylose, mannose, glucose, and galactose, with retention times of 15.921, 16.383, 16.63, 17.662, 27.687, 28.228, and 28.72 min, respectively. The results showed that CPP was mainly composed of rhamnose, arabinose, xylose, mannose, glucose, and galactose, and the molar ratio was 1.00 : 2.21 : 0.62 : 0.50 : 0.62 : 4.18, indicating that the main component of CPP was galactose.

*3.2. CPP Reduces the Proliferation Activity of Human Glioma Cell U251.* As shown in Figure 3, compared with the control group, U251 cells had a dose-dependent decrease in cell activity after 24, 48, and 72 h of 25, 50, 75, 100, 125, and 150 μmol/L CPP treatment ($p < 0.05$). When treated for 24 h with CPP (concentration was in the range of 25, 50, and 75 μmol/L), compared with the control group, U251 cell viability did not change significantly at each time point ($p > 0.05$). When the CPP concentration reached 100 μmol/L, cell viability was significantly reduced at all time points ($p < 0.05$). When treated with CPP (concentration was in the range of 25 and 50 μmol/L) for 48 and 72 h, compared with the control group, U251 cell viability did not change significantly at each time point ($p > 0.05$). When the CPP concentration reached 75 μmol/L, cell viability was significantly reduced at all time points ($p < 0.05$). And the longer the treatment time, the higher the degree of cell viability reduction. The numerical changes of specific cell viability are shown in Table 1. The above results suggest that CPP can inhibit the proliferation of U251 cells.

*3.3. CPP Induces Apoptosis of U251 Cells.* As shown in Figure 4, after U251 cells were treated with different concentrations of CPP (75, 100, 125, and 150 μmol/L) for 72 h, compared with the control group, the apoptosis rate increased with the increase of CPP treatment concentration ($p < 0.05$), as detailed in Table 2. The results suggest that the administration of CPP to U251 cells can induce the occurrence of apoptotic responses.

Table 2: Apoptosis of U251 cells under different concentrations of CPP treatment.

| Groups | Apoptosis rate (%) |
|---|---|
| Control | $6.17 \pm 0.70$ |
| CPP 75 μmol/L | $15.20 \pm 0.56^{*\#}$ |
| CPP 100 μmol/L | $25.40 \pm 0.70^{*\#}$ |
| CPP 125 μmol/L | $36.83 \pm 1.12^{*\#}$ |
| CPP 150 μmol/L | $50.67 \pm 2.30^{*\#}$ |

Note: compared with the control group, $^*p < 0.05$. Comparison between treatment groups with different concentrations of CPP (75, 100, 125, and 150 μmol/L), $\#p < 0.05$.

*3.4. CPP Treatment Reduces U251 Cell Migration Capacity.* As shown in Figure 5, after treating U251 cells with different concentrations of CPP (75, 100, 125, and 150 μmol/L) for 72 h, compared with the control group, the cell migration ability of the CPP-treated group was significantly reduced ($p < 0.05$) in a dose-dependent manner ($p < 0.05$).

*3.5. CPP Inhibits the Invasion of U251 Cells.* As shown in Figure 6, when U251 cells were exposed to different concentrations (75, 100, 125, and 150 μmol/L) of CPP, their invasion capacity was significantly reduced ($p < 0.05$). With the increase of the CPP treatment concentration, the cell invasion capacity declined in a dose-dependent manner ($p < 0.05$).

*3.6. CPP Inhibits Activation of the GSK3β/β-Catenin Signaling Pathway.* As shown in Figure 7, when U251 cells were treated with 150 μmol/L CPP for 72 h, the Western

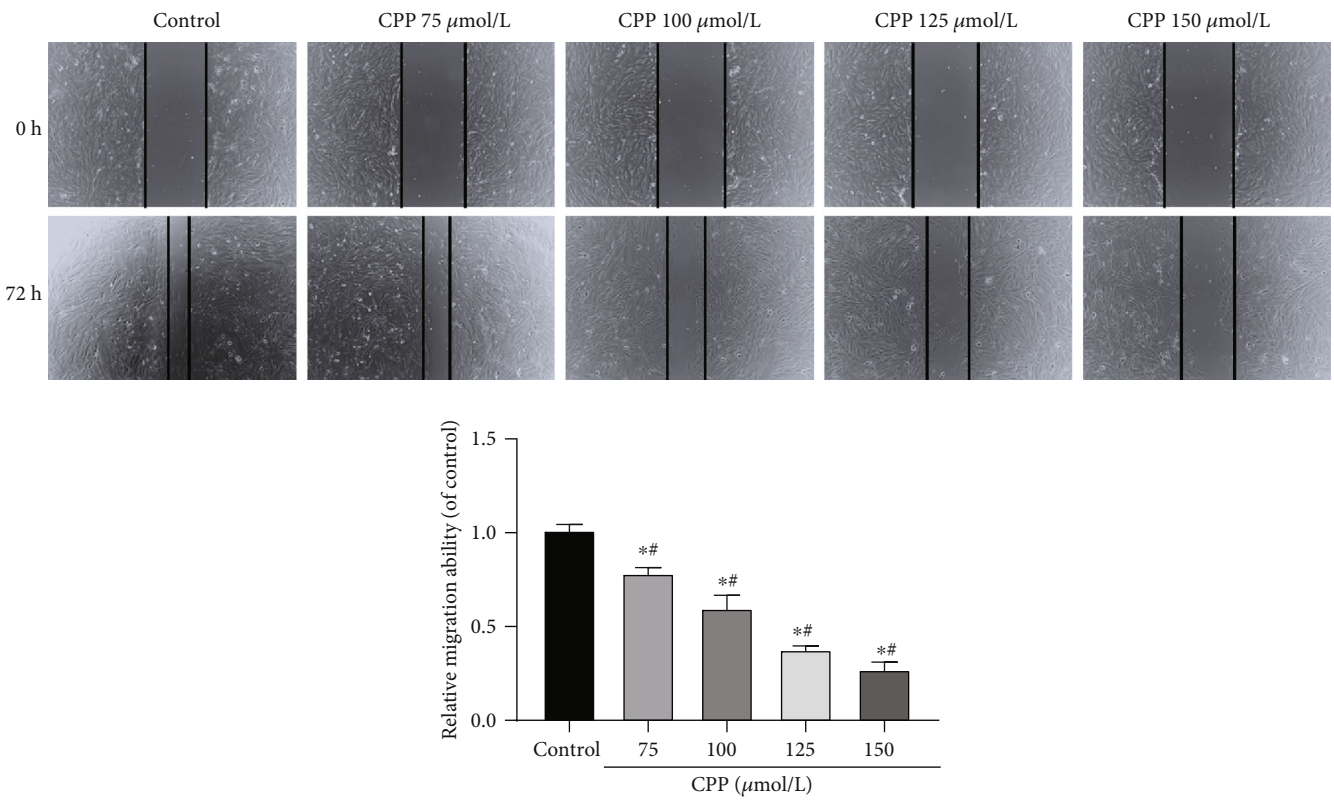


Figure 5: CPP treatment reduces U251 cell migration capacity. Compared with the control group, ∗ indicates $p < 0.05$. Comparison between treatment groups with different concentrations of CPP (75, 100, 125, and 150 μmol/L), # indicates $p < 0.05$. This experiment was repeated three times independently.

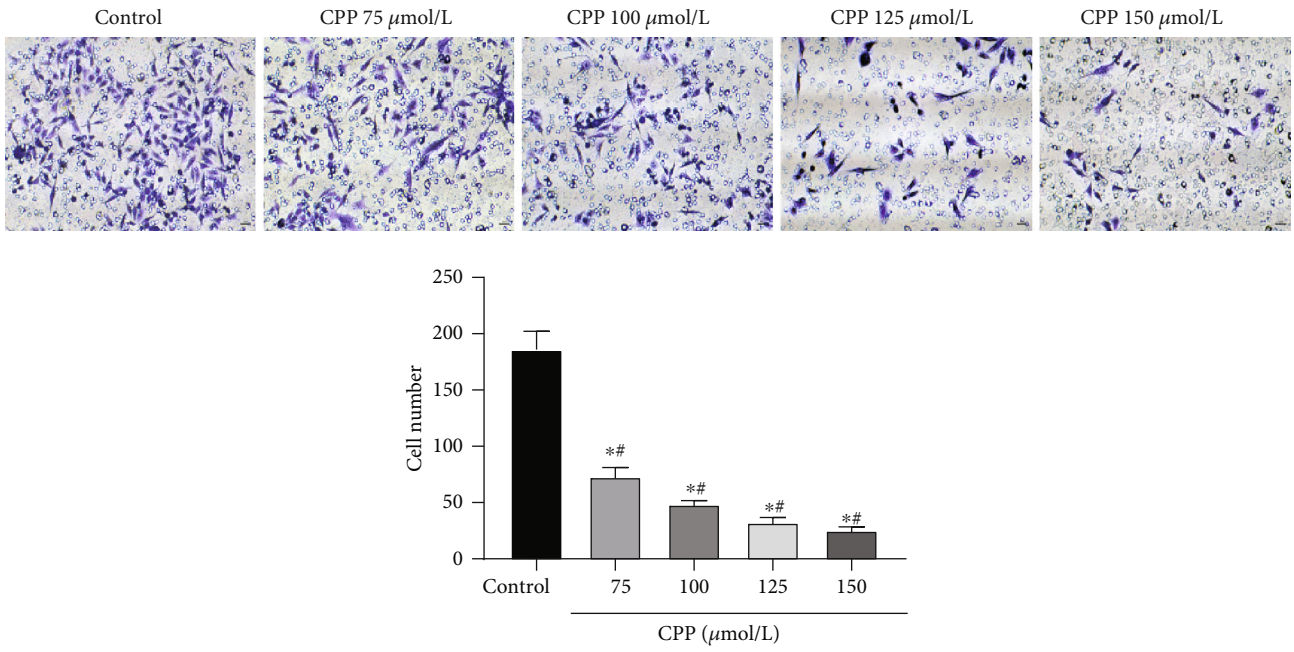


Figure 6: CPP treatment inhibits the invasion of U251 cells. Compared with the control group, ∗ indicates $p < 0.05$. Comparison between treatment groups with different concentrations of CPP (75, 100, 125, and 150 μmol/L), # indicates $p < 0.05$. The experiment was repeated three times independently.

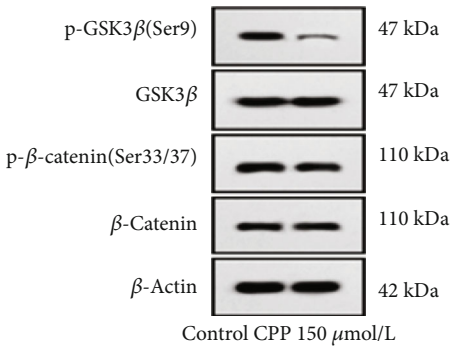


Figure 7: CPP inhibits GSK3$\beta$/$\beta$-catenin signaling pathway activation. Compared with the control group, $*$ indicates $p < 0.05$. This experiment was repeated three times independently.

blotting result showed that compared with the control group, CPP can significantly reduce the protein level of GSK3$\beta$ and its phosphorylation level at Ser9 site. Furthermore, treatment with CPP promotes the phosphorylation level of $\beta$-catenin at Ser33/37 site, leading to the degradation of $\beta$-catenin.

*3.7. CPP Inhibits the Expression of Oncogenes Downstream of the GSK3β/β-Catenin Signaling Pathway.* As shown in Figure 8, when U251 cells were treated with 150 $\mu$mol/L CPP for 72 h, compared with the control group, the mRNA and protein levels of Cyr61, CCND1, Vimentin, and Slug (proliferation, apoptosis, migration, and invasion related genes downstream of SK3$\beta$/$\beta$-catenin signaling pathway) were significantly reduced (all $p < 0.05$).

## 4. Discussion

As an edible and medicinal plant, *Cyclocarya paliurus* is widely used in the treatment of various diseases [15, 16]. The polysaccharide is the main active ingredient of *Cyclocarya paliurus* [14]. Polysaccharides, as natural biological macromolecules, have a variety of biological activities and are closely related to the maintenance of biological processes, for example, fungi and Ganoderma, which have inhibitory effects on tumor cells [17, 18]. There are few studies on the antitumor effect of CPP. This study found that CPP can play a positive role in the treatment of gliomas by inhibiting the activation of GSK3$\beta$/$\beta$-catenin signaling pathway and inhibiting the downstream gene expression related to proliferation, apoptosis, migration, and invasion.

Previous studies have confirmed that in colorectal cancer cells, CPP can work in combination with X-rays to inhibit the PI3K/Akt signaling pathway, thereby playing a role in inhibiting cancer cell proliferation and promoting apoptotic responses [12]; in addition, it has been found that CPP can increase the sensitivity of human non-small-cell lung cancer to radiotherapy [11], mainly by inhibiting the activation of the mTOR/Akt/PI3K signaling pathway. As there is no research report on CPP in glioma, we found for the first time in this study that CPP has a significant inhibitory effect on glioma, suggesting that CPP is expected to play a positive role in the clinical treatment of glioma.

GSK3$\beta$ is a serine-threonine kinase that can regulate signaling pathways involved in cell proliferation and cell cycle [19, 20]. Furthermore, GSK3$\beta$ also participates in tumorigenesis through Wnt/$\beta$-catenin. Studies have found that inhibition of GSK3$\beta$ can induce cell death in gliomas [21]. GSK3$\beta$ activity depends on its phosphorylation of serine 9. Under normal conditions, GSK3$\beta$ is nonphosphorylated and active. GSK3$\beta$ phosphorylation can interact with $\beta$-catenin and cause $\beta$-catenin degradation [22]. Conversely, if $\beta$-catenin degradation is inhibited, activation of oncogene can occur. Consistent with previous reports, this study confirms that CPP can inhibit the phosphorylation and protein levels of GSK3$\beta$ at Ser9, thereby promoting the phosphorylation of $\beta$-catenin at Ser33/37, leading to the degradation of $\beta$-catenin and thus inhibiting GSK3$\beta$/$\beta$-catenin signaling pathway activation.

At the same time, after we found that CPP can inhibit the proliferation, migration, and invasion of glioma cells through CCK-8, cell scratches, and Transwell experiments, we further investigated the mRNA expression and protein levels of oncogenes downstream of GSK3$\beta$/$\beta$-catenin signaling pathway including Cyr61, CCND1, Vimentin, and Slug which are related to proliferation and migration. Cyr61 is a cysteine-rich, secreted, heparin-binding protein that can participate in a variety of cellular functions such as adhesion, migration, and proliferation [23]. Previously, Xie et al. reported that compared with normal brain tissue, Cyr61 is highly expressed in 66 cases of primary glioma, and Cyr61 expression is significantly related to tumor grade and patient survival [24]; CCND1, as an oncogene [25], is highly expressed in glioma, breast, and bladder cancer; the expression level of CCND1 is related to the malignant degree of tumors and has the effect of regulating the growth and proliferation of cancer cells [26]; Vimentin can reduce the expression of cell surface adhesion factors, thereby promoting the occurrence of cell migration and invasion. It is highly expressed in a variety of cancer tissues, especially in cancers with metastasis [27]; Slug originated from the neural crest and has been reported to be involved in regulating tumor cell invasion, migration, cell cycle, and other activities [28]. In this study, qPCR and Western blotting experiments were performed to demonstrate that CPP treatment of U251 can cause the downregulation of mRNA and protein expression levels of Cyr61, CCND1, Vimentin, and Slug to different degrees, suggesting that CPP plays critical roles in regulating the proliferation, apoptosis, migration, and invasion of gliomas through inhibiting the expression of GSK3$\beta$/$\beta$-catenin downstream oncogenes Cyr61, CCND1, Vimentin, and Slug.

In this study, crude polysaccharides were first extracted from the leaves of *Cyclocarya paliurus*, and CPP was obtained after purification and drying. Through a series of in vitro experiments based on glioma cells U251, it was found that CPP has a certain cytotoxic effect to inhibit cell proliferation, apoptosis, migration, and invasion. In addition, in the mechanism research, we also found that CPP can inhibit the

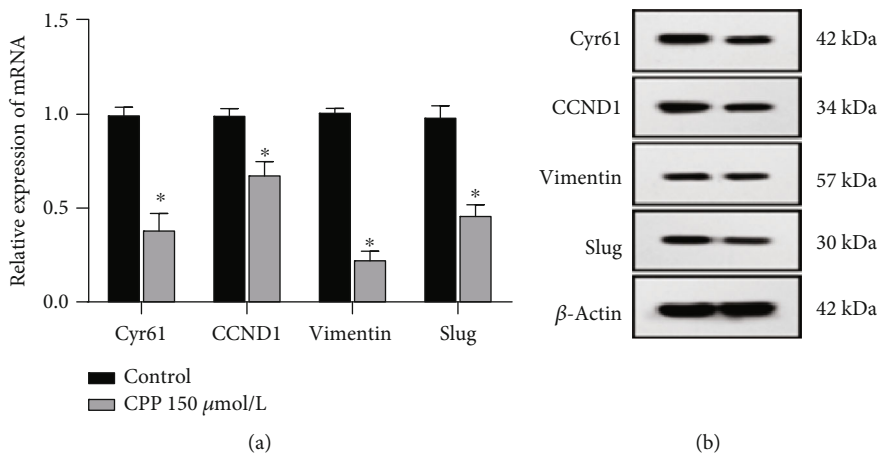


Figure 8: CPP inhibits the expression of oncogenes downstream of the GSK3$\beta$/$\beta$-catenin signaling pathway. Compared with the control group, $*$ indicates $p < 0.05$. This experiment was repeated three times independently.

activation of GSK3$\beta$/$\beta$-catenin signaling pathway. Furthermore, through the inhibition of the GSK3$\beta$/$\beta$-catenin signaling pathway, CPP can reduce the expression level of proliferation, apoptosis, migration, and invasion related genes such as Cyr61 and CCND1. All these results indicate that CPP may play a protective role in the treatment of gliomas, which deserves further study.

## Data Availability

All the data is available with the handwritten notebook documented in our lab.

## Conflicts of Interest

The authors declare that there are no conflicts of interest regarding the publication of this paper.

## Acknowledgments

This work is supported by Weifang Science and Technology Development Plan Project (Grant no. 2019YX040).

## References

[1] L. Ryskalin, A. Gaglione, F. Limanaqi et al., "The autophagy status of cancer stem cells in gliobastoma multiforme: from cancer promotion to therapeutic strategies," *International Journal of Molecular Sciences*, vol. 20, no. 15, p. 3824, 2019.

[2] C. H. Xu, L. M. Xiao, Y. Liu et al., "The lncRNA HOXA11-AS promotes glioma cell growth and metastasis by targeting miR-130a-5p/HMGB2," *European Review for Medical and Pharmacological Sciences*, vol. 23, no. 1, pp. 241–252, 2019.

[3] R. L. Siegel, K. D. Miller, and A. Jemal, "Cancer statistics, 2017," *CA: a Cancer Journal for Clinicians*, vol. 67, no. 1, pp. 7–30, 2017.

[4] M. N. A. Kamarudin and I. Parhar, "Emerging therapeutic potential of antipsychotic drugs in the management of human glioma: a comprehensive review," *Oncotarget*, vol. 10, no. 39, pp. 3952–3977, 2019.

[5] Q. Li, J. Hu, J. Xie, S. Nie, and M. Y. Xie, "Isolation, structure, and bioactivities of polysaccharides from Cyclocarya paliurus (Batal.) Iljinskaja," *Annals of the New York Academy of Sciences*, vol. 1398, no. 1, pp. 20–29, 2017.

[6] Z. J. Wang, J. H. Xie, M. Y. Shen et al., "Carboxymethylation of polysaccharide from Cyclocarya paliurus and their characterization and antioxidant properties evaluation," *Carbohydrate Polymers*, vol. 136, pp. 988–994, 2016.

[7] L. Xiong, K. H. Ouyang, Y. Jiang et al., "Chemical composition of _Cyclocarya paliurus_ polysaccharide and inflammatory effects in lipopolysaccharide-stimulated RAW264.7 macrophage," *International Journal of Biological Macromolecules*, vol. 107, no. Part B, pp. 1898–1907, 2018.

[8] Y. Yu, M. Shen, Z. Wang, Y. Wang, M. Xie, and J. Xie, "Sulfated polysaccharide from _Cyclocarya paliurus_ enhances the immunomodulatory activity of macrophages," *Carbohydrate Polymers*, vol. 174, pp. 669–676, 2017.

[9] Z. Yang, J. Wang, J. Li et al., "Antihyperlipidemic and hepatoprotective activities of polysaccharide fraction from _Cyclocarya paliurus_ in high-fat emulsion-induced hyperlipidaemic mice," *Carbohydrate Polymers*, vol. 183, pp. 11–20, 2018.

[10] Z. Yang, J. Zhao, J. Wang, J. Li, K. Ouyang, and W. Wang, "Effects of _Cyclocarya paliurus_ polysaccharide on lipid metabolism-related genes DNA methylation in rats," *International Journal of Biological Macromolecules*, vol. 123, pp. 343–349, 2019.

[11] Z. W. Yang, K. H. Ouyang, J. Zhao, H. Chen, L. Xiong, and W. J. Wang, "Structural characterization and hypolipidemic effect of Cyclocarya paliurus polysaccharide in rat," *International Journal of Biological Macromolecules*, vol. 91, pp. 1073–1080, 2016.

[12] Y. Jin, Z. Jin, and S. Jiang, "Antiproliferative and proapoptotic effects of Cyclocarya paliurus polysaccharide and X-ray irradiation combination on SW480 colorectal cancer cells," *Molecular Medicine Reports*, vol. 20, no. 4, pp. 3535–3542, 2019.

[13] F. Zhang, B. Fan, and L. Mao, "Radiosensitizing effects of Cyclocarya paliurus polysaccharide on hypoxic A549 and H520 human non-small cell lung carcinoma cells," *International Journal of Molecular Medicine*, vol. 44, no. 4, pp. 1233–1242, 2019.

[14] Z. Wu, T. Gao, R. Zhong et al., "Antihyperlipidaemic effect of triterpenic acid-enriched fraction from Cyclocarya paliurus leaves in hyperlipidaemic rats," *Pharmaceutical Biology*, vol. 55, no. 1, pp. 712–721, 2017.

[15] C. Jiang, Q. Wang, Y. Wei et al., "Cholesterol-lowering effects and potential mechanisms of different polar extracts from Cyclocarya paliurus leave in hyperlipidemic mice," *Journal of Ethnopharmacology*, vol. 176, pp. 17–26, 2015.

[16] J. H. Xie, X. Liu, M. Y. Shen et al., "Purification, physicochemical characterization and anticancer activity of a polysaccharide from Cyclocarya paliurus leaves," *Food Chemistry*, vol. 136, no. 3-4, pp. 1453–1460, 2013.

[17] Y. Hou, X. Ding, W. Hou et al., "Pharmacological evaluation for anticancer and immune activities of a novel polysaccharide isolated from Boletus speciosus Frost," *Molecular Medicine Reports*, vol. 9, no. 4, pp. 1337–1344, 2014.

[18] C. Wang, S. Shi, Q. Chen et al., "Antitumor and immunomodulatory activities of Ganoderma lucidum polysaccharides in glioma-bearing rats," *Integrative Cancer Therapies*, vol. 17, no. 3, pp. 674–683, 2018.

[19] B. W. Doble and J. R. Woodgett, "GSK-3: tricks of the trade for a multi-tasking kinase," *Journal of Cell Science*, vol. 116, Part 7, pp. 1175–1186, 2003.

[20] C. A. Grimes and R. S. Jope, "The multifaceted roles of glycogen synthase kinase 3beta in cellular signaling," *Progress in Neurobiology*, vol. 65, no. 4, pp. 391–426, 2001.

[21] S. Kotliarova, S. Pastorino, L. C. Kovell et al., "Glycogen synthase kinase-3 inhibition induces glioma cell death through c-MYC, nuclear factor-$\kappa$B, and glucose regulation," *Cancer Research*, vol. 68, no. 16, pp. 6643–6651, 2008.

[22] D. J. Mulholland, S. Dedhar, H. Wu, and C. C. Nelson, "PTEN and GSK3$\beta$: key regulators of progression to androgen-independent prostate cancer," *Oncogene*, vol. 25, no. 3, pp. 329–337, 2006.

[23] G. P. Yang and L. F. Lau, "Cyr61, product of a growth factor-inducible immediate early gene, is associated with the extracellular matrix and the cell surface," *Cell Growth & Differentiation*, vol. 2, no. 7, pp. 351–357, 1991.

[24] D. Xie, D. Yin, H. J. Wang et al., "Levels of expression ofCYR61andCTGFAre prognostic for tumor progression and survival of individuals with gliomas," *Clinical Cancer Research*, vol. 10, no. 6, pp. 2072–2081, 2004.

[25] R. Donnellan and R. Chetty, "Cyclin D1, and human neoplasia," *Molecular Pathology*, vol. 51, no. 1, pp. 1–7, 1998.

[26] L. Ma and J. Li, "MicroRNA-519d-3p inhibits cell proliferation and cell cycle G1/S transition in glioma by targeting CCND1," *Bioscience, Biotechnology, and Biochemistry*, vol. 84, no. 2, pp. 297–304, 2019.

[27] A. Satelli and S. Li, "Vimentin in cancer and its potential as a molecular target for cancer therapy," *Cellular and Molecular Life Sciences*, vol. 68, no. 18, pp. 3033–3046, 2011.

[28] X. Liu, S. Min, N. Wu et al., "miR-193a-3p inhibition of the Slug activator PAK4 suppresses non-small cell lung cancer aggressiveness via the p53/Slug/L1CAM pathway," *Cancer Letters*, vol. 447, pp. 56–65, 2019.

Hindawi
International Journal of Polymer Science
Volume 2020, Article ID 1934732, 8 pages
https://doi.org/10.1155/2020/1934732

*Research Article*

# Effect of $Mn_3O_4$ Nanoparticles on Lipopolysaccharide-Induced Inflammatory Factors in the Human Tendon Cells and Its Mechanism

**Shangjun Fu, Zongyun He, Yongfeng Tang, and Bo Lan**

*Hand and Foot Surgery, Yiwu Central Hospital, Yiwu, 322000 Zhejiang, China*

Correspondence should be addressed to Bo Lan; lanbo886@126.com

Received 3 January 2020; Accepted 17 February 2020; Published 4 March 2020

Guest Editor: Can Yang Zhang



*Objective*. To investigate the effect of $Mn_3O_4$ nanoparticles ($Mn_3O_4$NPs) on inflammatory factors induced by lipopolysaccharide (LPS) in human tendon cells and its mechanism. *Methods*. The $Mn_3O_4$NPs were synthesized by a hydrothermal method. RT-qPCR was used to detect the expression levels of miRNAs related to inflammation in human tendon cells. The expression level of NLRP1 (NOD-like receptor containing pyrin domain 1) was measured by Western blotting. ELISA assay was used to measure the level of TNF-$\alpha$, IL-1$\beta$, IL-4, and IL-10. The relationship between miR-181a-5p and NLRP1 was verified by dual-luciferase reporter assay. *Results*. $Mn_3O_4$NPs produced in this study were brown spherical particles with an average size of 7-10 nm. $Mn_3O_4$NP treatment significantly reduced the levels of TNF-$\alpha$ and IL-1$\beta$ but increased the levels of IL-4 and IL-10 in the human tendon cells induced by LPS. In addition, $Mn_3O_4$NP treatment remarkably increased the expression level of miR-181a-5p. NLRP1 is one of the targets of miR-181a-5p, and miR-181a-5p downregulated its expression. Further study showed that $Mn_3O_4$NPs could alleviate the inflammatory response of human tendon cells induced by LPS by upregulating miR-181a-5p and thus downregulating the expression of NLRP1. *Conclusion*. $Mn_3O_4$NPs affect the expression of inflammatory cytokines in the human tendon cells induced by LPS by modulating the molecular axis of miR-181a-5p/NLRP1.

## 1. Introduction

Tendonitis is the inflammation of the tendon caused by strain. It often occurs in the hands, wrists, shoulders, and knees. With the increasing use of computers, the hand controlling the mouse has been the most common hand which affected by tendonitis and its incidence has been increasing in recent years [1]. Recently, nanomaterials with new structures, new properties, and new functions have been widely used in the treatment of a variety of diseases including tumors [2], autoimmune diseases, etc. [3]; studies also shown that nanoparticles have good efficacy in the treatment of inflammation-related diseases [4]. Among them, $Mn_3O_4$ nanoparticles ($Mn_3O_4$NPs) have been demonstrated to alleviate inflammation of mouse ears induced by ROS [5]. Lipopolysaccharide (LPS), as a cell wall component of Gram-negative bacteria, has been often used to stimulate cells to produce inflammatory mediators to build a model of cellular inflammation. However, there are no reports about the effects of $Mn_3O_4$NPs on LPS-induced tendon inflammatory factor levels and their regulatory mechanisms. Therefore, in this study, to provide a new strategy for the treatment of tendonitis, human tendon cells were induced by LPS to form a tendinitis model, and the effect of $Mn_3O_4$NPs on the expression level of inflammatory factors was explored.

## 2. Material and Methods

*2.1. Cell Lines and Reagents.* Human tendon cells HT (Cat. No. PR203) were purchased from Beijing Fubo Biotechnology Co., Ltd. Fetal bovine serum, DMEM medium, penicillin, and streptomycin were purchased from Guangzhou Ruite Biotechnology Co., Ltd. $Mn(OAc)_2{\cdot}4H_2O$ and TRIzol one-

step RNA extraction reagents were purchased from Shanghai Yanjin Biotechnology Co., Ltd. The reverse transcription kit, total protein extraction kit, and dual-luciferase reporter gene detection kit were purchased from Wuhan Purity Biotechnology Co., Ltd. Lipofectamine 2000 kit was purchased from Shanghai Mingming Biotechnology Co., Ltd. TNF-$\alpha$, IL-1$\beta$, IL-4, and IL-10 ELISA kits were purchased from Shanghai Kemin Biotechnology Co., Ltd.

*2.2. Preparation and Identification of $Mn_3O_4$ Nanoparticles.* The low-temperature esterification method reported by Li et al. [6] was used to prepare $Mn_3O_4$ nanoparticles. Specifically, 1 g of Mn $(OAc)_2{\cdot}4H_2O$ was dissolved in 60 ml of absolute ethanol, stirring magnetically until completely dissolved, adding 100 ml of polytetrafluoroethylene, and placed in an autoclave at 120°C for processing. After 24 h, it was cooled to room temperature and washed with deionized water three times to obtain $Mn_3O_4$NPs. The transmission electron microscope (TEM) was used to observe the color, and a laser particle size analyzer was used for the analysis of the morphology and particle size of the prepared $Mn_3O_4$NPs. The prepared $Mn_3O_4$NPs were also analyzed with X-ray diffraction (XRD).

*2.3. Cell Culture and Transfection.* Human tendon cell HT was cultured in DMEM medium containing 10% fetal bovine serum, 100 U/l penicillin, and 100 mg/l streptomycin (containing 10% fetal bovine serum), at 37°C with 5% $CO_2$. Once the cell growth was stable, 1 mg/ml lipopolysaccharide (LPS) was added to build the human tendon cell inflammation model. After 24 h of treatment, miR-181a-5p mimics, miR-181a-5p inhibitor, and si-NLRP1 were transfected into cells according to the experimental design. The experimental groups included NC group (HT cells without transfection treatment), miR-181a-5p mimics group (overexpression of miR-181a-5p in HT cells), si-NLRP1 group (knockout NLRP1 in HT cells), and si-NLRP1+miR-181a-5p inhibitor group (simultaneously knockout NLRP1 and miR-181a-5p in HT cells). Lipofectamine 2000 kit was used for transfection according to the instructions. After 48 h, the transfected cells were collected for subsequent experiments.

*2.4. Determination of $Mn_3O_4$NP Cytotoxicity and Treatment of $Mn_3O_4$NPs.* MTT method was used to detect the cytotoxicity of $Mn_3O_4$NPs to HT cells. The HT cells were cultured in 96-well plates. After incubation overnight, the fresh medium was changed, and different concentrations (0, 2, 4, 6, 8, and 10 $\mu$g/ml) of $Mn_3O_4$NPs were added and incubated. After 48 hours of incubation, the fresh medium and MTT was added, and the absorbance of the cells at 570 nm was detected by a microplate reader to determine the cytotoxicity of $Mn_3O_4$NPs to HT cells. After cytotoxicity testing, HT cells in each experimental group were treated with 10 $\mu$g/ml $Mn_3O_4$NPs for 48 h.

*2.5. RT-qPCR.* Total RNA of cells in each experimental group was extracted by TRIzol one-step method. 2 $\mu$l of total RNA was reversely transcribed into cDNA according to the reverse transcription kit instructions. The reverse transcription product was placed in a PCR instrument for the reaction. The 20 $\mu$l reaction system contains 0.5 $\mu$l reverse transcription product, 1 $\mu$l upstream and downstream primers, 10 $\mu$l SYBR Premix Ex Taq, and 7.5 $\mu$l RNase-FREE water. The reaction conditions were 90°C for 10 min, 95°C for 30 s, and 55°C for 1 min. A total of 50 cycles were performed.

The primer sequences are as follows:

miR-181a-5p upstream primer sequence: 5′-CGGCAA CATTCAACGCTGT-3′;

miR-181a-5p downstream primer sequence: 5′-GTGC AGGGTCCGAGGTATTC-3′. U6 upstream primer sequence: 5′-CTTCGGCAGCACATATAC-3′; U6 downstream primer sequence: 5′-GAACGCTTCACGAATTTGC-3′.

Quantitative fluorescence detection results were calculated by the $2^{-\Delta\Delta Ct}$ method.

*2.6. Western Blotting.* The total protein of each experimental group was extracted using a total protein extraction kit. The equivalent amount of denatured protein sample was loaded, and SDS-PAGE electrophoresis was performed. After 2 h of electrophoresis, the membrane was transferred at 100 V. After the film is transferred, it was sealed in 5% skimmed milk powder. After 2 h, the membrane was washed, and a primary antibody (ani-NLRP1, 1 : 1000; ani-GAPDH, 1 : 1000) was added and incubated at 4°C overnight. The next day, after washing the membrane, a secondary antibody (1 : 1000) was added and incubated at room temperature for 2 h. After the reaction was complete, the film was washed, and a chemiluminescence developing solution was added for development and photographs. Grayscale analysis of protein bands was performed using ImageJ software.

*2.7. ELISA.* The cell supernatants of each experimental group were obtained by centrifugation, and the contents of TNF-$\alpha$, IL-1$\beta$, IL-4, and IL-10 were measured according to the instructions of the ELISA kit. In specific, 100 $\mu$l of the standard sample and the test sample were added to a 96-well plate and incubated at 37°C for 1 hour and rinsed with a washing solution. 100 $\mu$l of the primary antibody working solution was added to each well, mixed, and incubated at 37°C. After 1 h, the plate was washed; 100 $\mu$l enzyme-labeled antibody working solution was added and incubated at 37°C. After 30 minutes, the plate was washed again; 100 $\mu$l of substrate working solution was added and reacted at 37°C in the dark. After 15 min, 100 $\mu$l of reaction stop solution was added and samples were further incubated at 37°C for 10 min. After the reaction was completed, the OD value was measured by a microplate reader, and a standard curve was drawn to determine the contents of TNF-$\alpha$, IL-1$\beta$, IL-4, and IL-10 in the measured samples.

*2.8. Double Luciferase Reporter Assay.* The 3′-UTR fragments of the wild-type and mutant NLRP1 genes were amplified and inserted into a double luciferase reporter gene plasmid. The reporter gene plasmid and miR-181a-5p mimics were cotransfected into T293 cells and cultured. After 48 h, luciferase activity was measured.

*2.9. Statistical Analysis.* All experimental data in this study were expressed as $\bar{x} \pm s$. Analysis of data was performed using

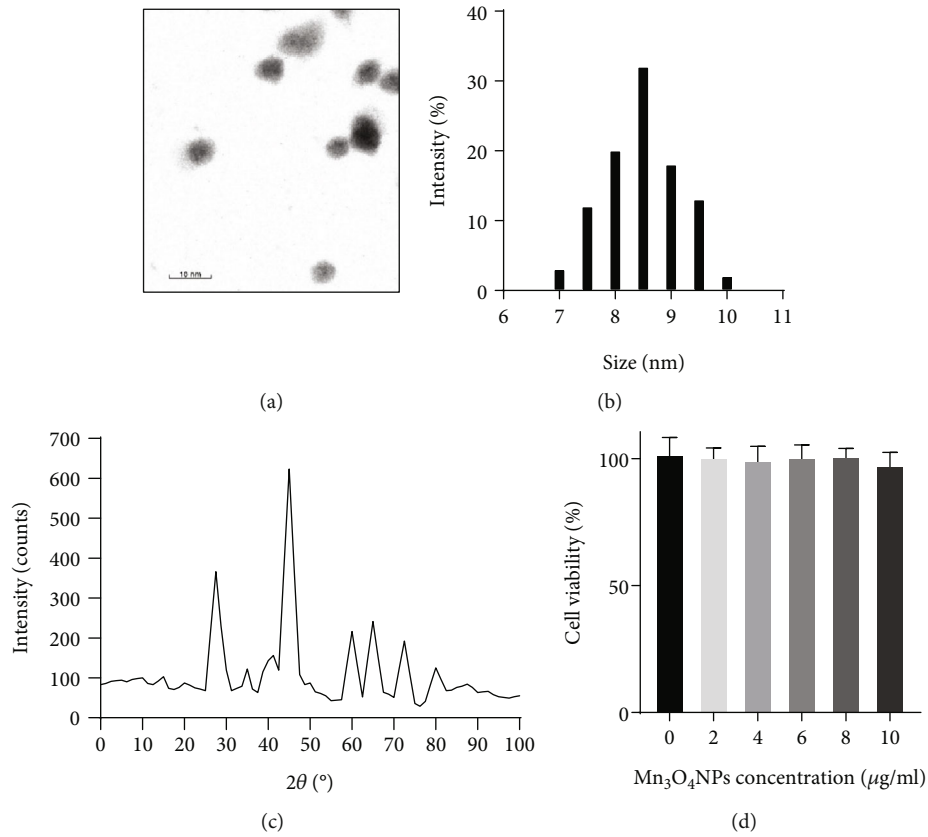


Figure 1: Identification of $Mn_3O_4$NPs and their cytotoxicity detection. (a) The morphology of $Mn_3O_4$NPs by transmission electron microscope. (b) The particle size distribution range of $Mn_3O_4$NPs analyzed by laser particle size analyzer. (c) T he XRD pattern of $Mn_3O_4$NPs detected by X-ray diffraction. (d) Detection of the cytotoxicity of $Mn_3O_4$NPs with MTT method.

SPSS 22.0. The $t$-test was used to compare the two groups, and the one-way analysis of variance was used to compare the multiple groups. $P < 0.05$ or $P < 0.01$ indicates that the difference is statistically significant.

## 3. Results

*3.1. Identification of $Mn_3O_4$ Nanoparticles and Detection of Their Cytotoxicity.* Observed with a transmission electron microscope, the prepared $Mn_3O_4$NPs were spherical particles, as shown in Figure 1(a). The particle size distribution of $Mn_3O_4$NPs analyzed by laser particle size analyzer was about 7-10 nm, as shown in Figure 1(b). X-ray diffraction analysis results showed that the prepared $Mn_3O_4$NPs diffraction peaks are in good concordance with the $Mn_3O_4$ standard chart (JCPDS card No. 24-0734) and do not contain impurity peaks as shown in Figure 1(c), which was used in subsequent experiments. The results of the MTT assay showed that $Mn_3O_4$NPs had no significant toxicity to HT cells in the experimental range, as shown in Figure 1(d).

*3.2. Effects of $Mn_3O_4$ Nanoparticles on Inflammatory Factors in Human Tendon Cells Induced by LPS.* ELISA results showed that the expression levels of TNF-$\alpha$ and IL-1$\beta$ in HT cells were significantly increased after LPS induction ($P < 0.01$), and the expression levels of IL-4 and IL-10 were significantly decreased ($P < 0.01$). Compared with the LPS group, $Mn_3O_4$NP treatment significantly reduced the expression levels of TNF-$\alpha$ and IL-1$\beta$ in cells ($P < 0.05$), and significantly increased the expression levels of IL-4 and IL-10 ($P < 0.05$) (Figure 2). Therefore, $Mn_3O_4$NP treatment significantly inhibited LPS-induced human tendon cell inflammation.

*3.3. Effects of $Mn_3O_4$ Nanoparticles on the Expression Level of Inflammation-Related miRNA in Human Tendon Cell-Induced LPS.* RT-PCR results showed that $Mn_3O_4$NPs affected the expression level of inflammation-related miRNAs in HT cells induced by LPS, and the expression level of miR-181a-5p was significantly higher than that of the untreated group, as shown in Figure 3. The mechanism of miR-181a-5p affecting LPS-induced inflammation of human tendon cells was further explored in subsequent experiments.

*3.4. Targeting Relationship between miR-181a-5p and NLRP1.* The StarBase database was used to predict the binding sites of NLRP1 and miR-181a-5p as shown in Figure 4(a). The results of the double luciferase experiment showed that miR-181a-5p mimics significantly reduced the luciferase activity of the NLRP1 wild-type vector ($P < 0.05$), but had no effect on the luciferase activity of the NLRP1 mutant vector (Figure 4(b)). In addition, Western blotting results showed that overexpression of miR-181a-5p significantly reduced the expression level of NLRP1 protein in LPS-

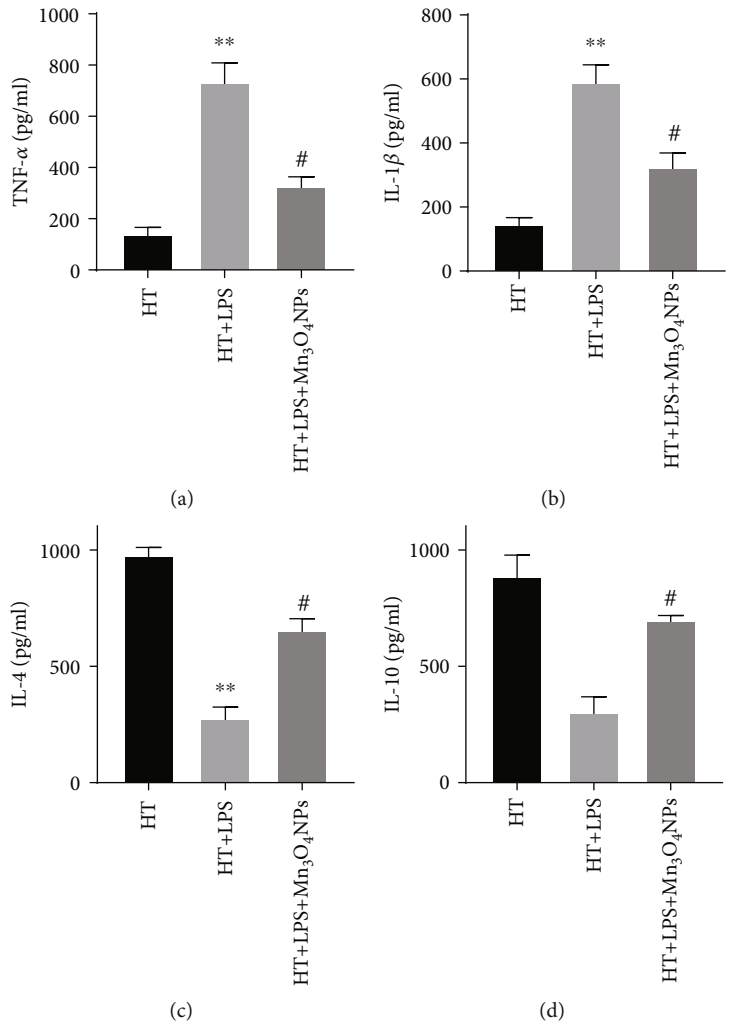


Figure 2: Effects of $Mn_3O_4$ nanoparticles on the inflammatory factors levels in human tendon cells induced by LPS. (a) TNF-$\alpha$ level measured by ELISA. (b) IL-1$\beta$ level measured by ELISA. (c) IL-4 level measured by ELISA. (d) IL-10 level measured by ELISA. $^{**}P < 0.01$ vs. HT group; $^{\#}P < 0.05$ vs. HT+LPS group.

induced HT cells ($P < 0.05$) (Figure 4(c)). From these results, it seemed that there is a targeting relationship between miR-181a-5p and NLRP1 in LPS-induced human tendon cells and miR-181a-5p downregulated the NLRP1 expression.

*3.5. Mechanism of $Mn_3O_4$ Nanoparticles Affecting LPS-Induced Inflammatory Factors in Human Tendon Cells.* ELISA results showed that knockout of NLRP1 significantly reduced the expression levels of TNF-$\alpha$ and IL-1$\beta$ in HT cells induced by LPS ($P < 0.01$) and significantly increased the expression levels of IL-4 and IL-10 ($P < 0.01$). Compared with the NLRP1 knockout group, the treatment of NLRP1 knockout with $Mn_3O_4$NPs significantly reduced the expression levels of TNF-$\alpha$ and IL-1$\beta$ ($P < 0.05$) and at the time significantly increased the expression levels of IL-4 and IL-10 ($P < 0.05$). The expression levels of TNF-$\alpha$ and IL-1$\beta$ in the si-NLRP1+$Mn_3O_4$NPs+miR-181a-5p inhibitor group were higher than those in the si-NLRP1+$Mn_3O_4$NPs group ($P < 0.05$), and the expression levels of IL-4 and IL-10 were lower than si-NLRP1+$Mn_3O_4$NPs group ($P < 0.05$). Compared with the si-NLRP1+$Mn_3O_4$NPs+miR-181a-5p inhibitor group, the expression levels of TNF-$\alpha$ and IL-1$\beta$ were increased in the $Mn_3O_4$NPs+miR-181a-5p inhibitor group ($P < 0.05$), whereas IL-4 and IL expression levels were decreased ($P < 0.05$) (Figure 5). From the above experimental results, it seems that $Mn_3O_4$NPs upregulated miR-181a-5p in HT cells induced by LPS to downregulate the expression of NLRP1, thereby inhibiting LPS-induced HT cell inflammation.

## 4. Discussion

Tendonitis can cause abnormalities in the normal biological properties of tendons, such as thickening of the tendon and damage of the synovium, and the pain caused by it severely affects the daily activities of patients [7]. As the hands are the main organ for daily labor, the tendon of the hands is extremely susceptible to cumulative strain; therefore, hand tendinitis is also very common in clinical practice [8]. Local hormone injection is currently the most commonly used method of treating tendinitis, but studies have shown that local hormone injection has the risk of causing necrosis of

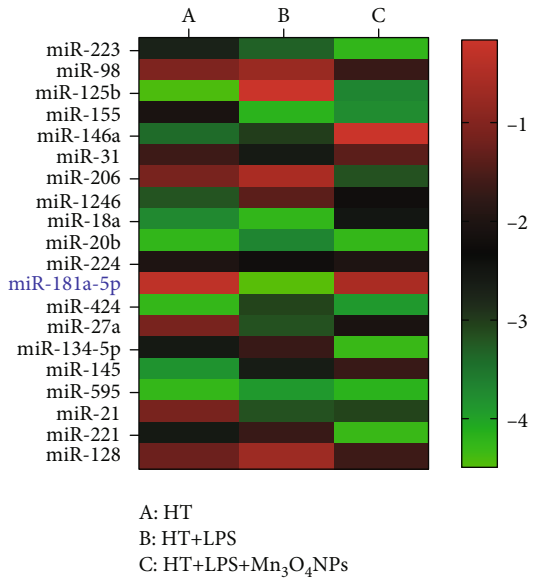


Figure 3: $Mn_3O_4$ nanoparticles effect on the expression of inflammatory-related miRNA in human tendon cells induced by LPS.

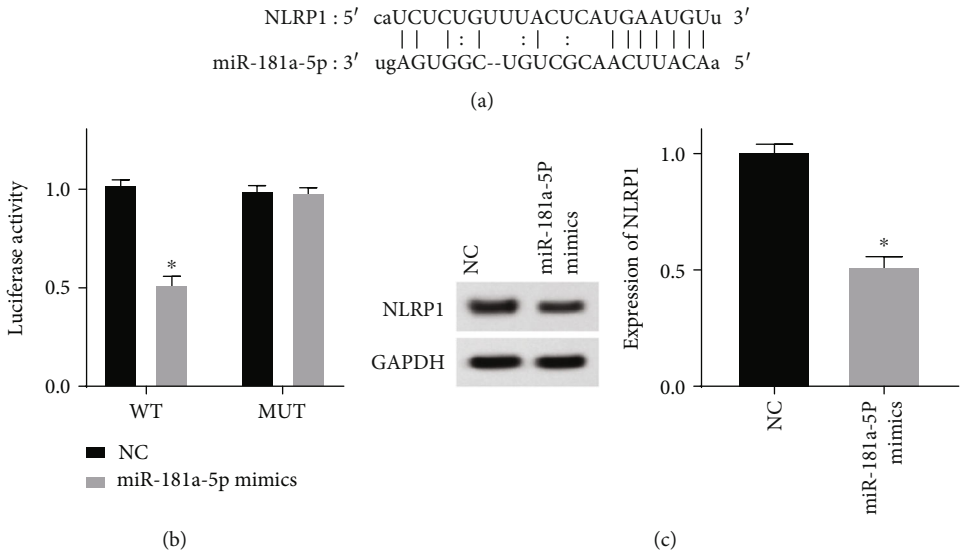


Figure 4: Relationship between miR-181a-5p and NLRP1. (a) Binding sites between miR-181a-5p and NLRP1 predicted by StarBase. (b) The interaction of miR-181a-5p and NLRP1 determined by dual-luciferase reporter assay. (c) NLRP1 expression level measured by western blotting. $^*P < 0.01$ vs. NC group.

tendon collagen [9]. In recent years, with the in-depth study of nanoparticles, its important role in the treatment of inflammation-related diseases has also been confirmed [10].

$Mn_3O_4$NPs, as nanomaterials with enzyme-like activity, display good therapeutic potential in the treatment of inflammatory diseases. Studies have confirmed that $Mn_3O_4$NPs can functionally mimic superoxide dismutase (SOD), catalase (CAT), and glutathione peroxidase (GPX), and can significantly remove superoxide anion radicals and peroxidation hydrogen and hydroxyl radicals to protect cells from oxidative damage [11]. ROS imbalances including superoxide anion free radicals, hydrogen peroxide, and hydroxyl free radicals often occurred in inflammation. Therefore, $Mn_3O_4$NPs with high active oxygen scavenging activity and high stability have been shown to significantly relieve ROS-induced mouse ear inflammatory response [12]. However, there are few reports about $Mn_3O_4$NPs in the treatment of inflammation, and the research on its mechanism of action is lacking. The results of this study indicate that $Mn_3O_4$NPs significantly reduced the levels of proinflammatory-related proteins in human tendon cells induced by LPS and increased the levels of anti-inflammatory-related proteins to alleviate the inflammatory response.

MicroRNAs (miRNAs), as a class of noncoding single-stranded small RNAs composed of 19 to 22 nucleotides, can target mRNAs to degrade them or inhibit the translation

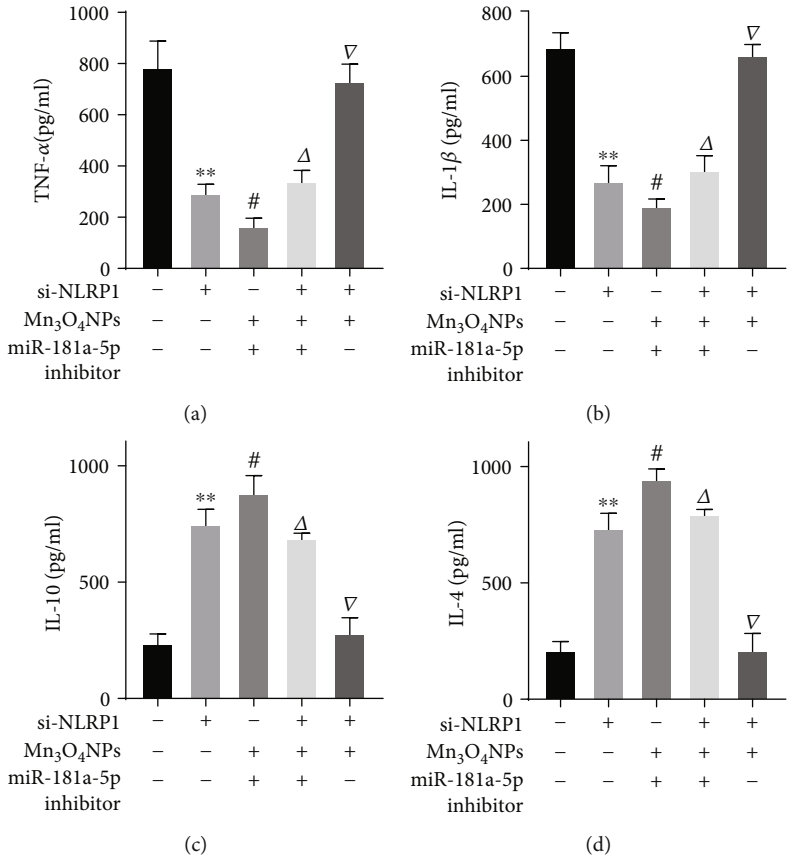


Figure 5: Mechanism of $Mn_3O_4$ nanoparticles effect on the inflammatory factors levels in human tendon cells induced by LPS. (a) TNF-$\alpha$ level measured by ELISA. (b) IL-1$\beta$ level measured by ELISA. (c) IL-4 level measured by ELISA. (d) IL-10 level measured by ELISA. $^{**}P < 0.01$ vs. NC group; $^{\#}P < 0.05$ vs. si-NLRP1 group; $^{\Delta}P < 0.05$ vs. si-NLRP1+$Mn_3O_4$NPs group; $^{\nabla}P < 0.05$ vs. si-NLRP1 +$Mn_3O_4$NPs+miR-181a-5p inhibitor group.

process, thereby regulating the physiological processes of cells [13]. Many studies have confirmed that the occurrence and development of inflammatory-related diseases are closely associated with miRNAs [14]. For instance, studies have shown that the expression level of miRNA-146a is positively correlated with the severity of the inflammatory response and can be used as an indicator of the inflammatory response disease activity [15]. Studies by Marques-Rocha et al. [13] showed that continuously upregulated miR-155 can also lead to sustained inflammatory responses. Among them, miR-181a has also been shown to be associated with inflammation. Studies have shown that miR-181a can significantly inhibit the expression of inflammatory factors IL-1$\beta$, IL-6, and TNF-$\alpha$ in macrophages induced by LPS [16]. In addition, miR-181a can also affect the myometrial inflammatory response by regulating the expression levels of ER-$\alpha$ and c-Fos [17]. Studies have also illustrated that miR-181a participates in the homeostatic response to inflammatory stimuli by regulating the TLR-4 signaling pathway [18]. The experimental results of this study also confirmed that miR-181a-5p is involved in regulating the expression of inflammatory factors in human tendon cells induced by LPS.

miRNAs play an important role in the occurrence and development of inflammatory diseases by binding to target genes and regulating the expression of target proteins related to inflammation. The association of NLRP1 with inflammation has been demonstrated [19]. NLRP1 is widely present in T cells, B cells, macrophages, and dendritic cells. When not stimulated, NLRP1 leucine-rich repeat-rich domains bind to the central nucleotide-binding oligomerization regions (NACHT), self-oligomerization is inhibited and in an inactive state. Upon stimulation, its domain changes, and it binds to proteins such as apoptosis-related speckle-like protein (ASC) and semi-aspartase (caspase-1) to form a protein complex called an inflammasome, which can regulate the interleukin expression level, activates the NF-$\kappa$B and MAPK signaling pathways, and participates in the body's inflammatory response [20]. The proven proinflammatory factors including tumor necrosis factor-$\alpha$ (TNF-$\alpha$) produced by monocyte macrophages function in immune regulation, participate in fever and inflammation, and can further induce the production of other cytokines [21]. Interleukin-1$\beta$ (IL-1$\beta$), as a pleiotropic factor, is the main mediator of the host's response to infection or tissue damage [22]. And the immune factors, especially the imbalance of Th1/Th2 immune response, often occur in the inflammatory response, among which interleukin-4 (IL-4) and interleukin-10 (IL-4) produced by the Th2 subset of CD4+ T cells. IL-10 has been shown to increase expression levels in the inflammatory response [23]. Studies have demonstrated that in rat

tendon cell inflammation models, stimulating factors can promote the activation of NLRP inflammasomes by disaggregating cytoskeleton F-actin, thereby increasing the expression and release of inflammatory factors TNF-$\alpha$, IL-6, and IL-1$\beta$ to aggravate the development of inflammation [24]. The results of this study indicate that miR-181a-5p downregulated NLRP1 expression in human tendon cells induced by LPS, and knocking out NLRP1 significantly alleviated the inflammatory response of human tendon cells induced by LPS.

The results of this study indicate that $Mn_3O_4$NP treatment can significantly reduce the levels of proinflammatory factors TNF-$\alpha$ and IL-1$\beta$ in human tendon cells induced by LPS and increase the levels of IL-4 and IL-10. Further research confirmed that $Mn_3O_4$NPs upregulated miR-181a-5p in human tendon cells induced by LPS, and by doing that downregulated the expression of NLRP1 thus alleviating the LPS-induced human tendon cell inflammation.

## Data Availability

All the data are available with the handwritten notebook documented in our lab.

## Conflicts of Interest

The authors declare that there are no conflicts of interest regarding the publication of this paper.

## Acknowledgments

This work is supported by the 2017 Yiwu General Scientific Research Project (No. 17-1-13).

## References

[1] L. Padua, D. Coraci, C. Erra et al., "Carpal tunnel syndrome: clinical features, diagnosis, and management," *Lancet Neurology*, vol. 15, no. 12, pp. 1273–1284, 2016.

[2] J. Ding, J. Chen, L. Gao et al., "Engineered nanomedicines with enhanced tumor penetration," *Nano Today*, vol. 29, article 100800, 2019.

[3] X. Feng, W. Xu, Z. Li, W. Song, J. Ding, and X. Chen, "Immunomodulatory nanosystems," *Advanced Science*, vol. 6, no. 17, article 1900101, 2019.

[4] Q. Zhang, D. Dehaini, Y. Zhang et al., "Neutrophil membrane-coated nanoparticles inhibit synovial inflammation and alleviate joint damage in inflammatory arthritis," *Nature Nanotechnology*, vol. 13, no. 12, pp. 1182–1190, 2018.

[5] J. Yao, Y. Cheng, M. Zhou et al., "ROS scavenging $Mn_3O_4$ nanozymes for *in vivo* anti-inflammation," *Chemical Science*, vol. 9, no. 11, pp. 2927–2933, 2018.

[6] X. Q. Li, L. P. Zhou, J. Gao, H. Miao, H. Zhang, and J. Xu, "Synthesis of $Mn_3O_4$ nanoparticles and their catalytic applications in hydrocarbon oxidation," *Powder Technology*, vol. 190, no. 3, pp. 324–326, 2009.

[7] L. Gaut and D. Duprez, "Tendon development and diseases," *Wiley Interdisciplinary Reviews: Developmental Biology*, vol. 5, no. 1, pp. 5–23, 2016.

[8] E. R. Wagner and M. B. Gottschalk, "Tendinopathies of the forearm, wrist, and hand," *Clinics in Plastic Surgery*, vol. 46, no. 3, pp. 317–327, 2019.

[9] J. C. Kennedy and R. B. Willis, "The effects of local steroid injections on tendons: a biomechanical and microscopic correlative study," *The American Journal of Sports Medicine*, vol. 4, no. 1, pp. 11–21, 1976.

[10] C. Dianzani, F. Foglietta, B. Ferrara et al., "Solid lipid nanoparticles delivering anti-inflammatory drugs to treat inflammatory bowel disease: effects in an in model," *World Journal of Gastroenterology*, vol. 23, no. 23, pp. 4200–4210, 2017.

[11] N. Singh, M. A. Savanur, S. Srivastava, P. D'Silva, and G. Mugesh, "A redox modulatory $Mn_3O_4$ nanozyme with multi-enzyme activity provides efficient cytoprotection to human cells in a Parkinson's disease model," *Angewandte Chemie*, vol. 56, no. 45, pp. 14267–14271, 2017.

[12] M. Zendjabil, S. Favard, C. Tse, O. Abbou, and B. Hainque, "The microRNAs as biomarkers: what prospects?," *Comptes Rendus Biologies*, vol. 340, no. 2, pp. 114–131, 2017.

[13] J. L. Marques-Rocha, M. Samblas, F. I. Milagro, J. Bressan, J. A. Martínez, and A. Marti, "Noncoding RNAs, cytokines, and inflammation-related diseases," *The FASEB Journal*, vol. 29, no. 9, pp. 3595–3611, 2015.

[14] Y. Tan, L. Yu, C. Zhang, K. Chen, J. Lu, and L. Tan, "miRNA-146a attenuates inflammation in an *in vitro* spinal cord injury model via inhibition of TLR4 signaling," *Experimental and Therapeutic Medicine*, vol. 16, no. 4, pp. 3703–3709, 2018.

[15] S. Bala, T. Csak, B. Saha et al., "The pro-inflammatory effects of miR-155 promote liver fibrosis and alcohol-induced steatohepatitis," *Journal of Hepatology*, vol. 64, no. 6, pp. 1378–1387, 2016.

[16] X. J. Du, J. M. Lu, and Y. Sha, "MiR-181a inhibits vascular inflammation induced by ox-LDL via targeting TLR4 in human macrophages," *Journal of Cellular Physiology*, vol. 233, no. 10, pp. 6996–7003, 2018.

[17] L. Gao, G. Wang, W. N. Liu, H. Kinser, H. L. Franco, and C. R. Mendelson, "Reciprocal feedback between miR-181a and E2/ER$\alpha$ in myometrium enhances inflammation leading to labor," *The Journal of Clinical Endocrinology and Metabolism*, vol. 101, no. 10, pp. 3646–3656, 2016.

[18] H. Li, G. di, Y. Zhang, R. Xue, J. Zhang, and J. Liang, "MicroRNA-155 and microRNA-181a, via HO-1, participate in regulating the immunotoxicity of cadmium in the kidneys of exposed *Cyprinus carpio*," *Fish & Shellfish Immunology*, vol. 95, pp. 473–480, 2019.

[19] C. H. Yu, J. Moecking, M. Geyer, and S. L. Masters, "Mechanisms of NLRP1-mediated autoinflammatory disease in humans and mice," *Journal of Molecular Biology*, vol. 430, no. 2, pp. 142–152, 2018.

[20] R. Liu, A. D. Truax, L. Chen et al., "Expression profile of innate immune receptors, NLRs and AIM2, in human colorectal cancer: correlation with cancer stages and inflammasome components," *Oncotarget*, vol. 6, no. 32, pp. 33456–33469, 2015.

[21] D. Li, D. Chen, X. Zhang et al., "c-Jun N-terminal kinase and Akt signalling pathways regulating tumour necrosis factor-$\alpha$-induced interleukin-32 expression in human lung fibroblasts: implications in airway inflammation," *Immunology*, vol. 144, no. 2, pp. 282–290, 2015.

[22] D. Gleiznys, A. Gleiznys, L. Abraškevičiūtė, A. Vitkauskienė, V. Šaferis, and J. Sakalauskienė, "Interleukin-10 and interleukin-1$\beta$ cytokines expression in leukocytes of patients with chronic peri-mucositis," *Medical Science Monitor*, vol. 25, pp. 7471–7479, 2019.

[23] G. R. Gandhi, M. T. S. L. Neta, R. G. Sathiyabama et al., "Flavonoids as Th1/Th2 cytokines immunomodulators: a systematic review of studies on animal models," *Phytomedicine*, vol. 44, pp. 74–84, 2018.

[24] Q. Chen, J. Zhou, B. Zhang, Z. Chen, Q. Luo, and G. Song, "Cyclic stretching exacerbates tendinitis by enhancing NLRP3 inflammasome activity via F-actin depolymerization," *Inflammation*, vol. 41, no. 5, pp. 1731–1743, 2018.